Large, long range tensile forces drive convergence during *Xenopus* blastopore closure and body axis elongation.

David R. Shook[1], Eric M. Kasprowicz[2], Lance A. Davidson[3], and Ray Keller[1]

[1]Dept. of Biology, University of Virginia, Charlottesville, VA

[2]Dept. of Internal Medicine, Thomas Jefferson University Hospital, Philadelphia, PA

[3]Depts. of Bioengineering, Developmental Biology, and Computational and Systems Biology, University of Pittsburgh, Pittsburgh, PA

ABSTRACT

Indirect evidence suggests that blastopore closure during gastrulation of anamniotes, including amphibians such as *Xenopus laevis*, depends on circumblastoporal convergence forces generated by the marginal zone (MZ), but direct evidence is lacking. We show that explanted MZs generate tensile convergence forces up to 1.5 μN during gastrulation and over 4 μN thereafter. These forces are generated by convergent thickening (CT) until the midgastrula and increasingly by convergent extension (CE) thereafter. Explants from ventralized embryos, which lack tissues expressing CE but close their blastopores, produce up to 2 μN of tensile force, showing that CT alone generates forces sufficient to close the blastopore. Uniaxial tensile stress relaxation assays show stiffening of mesodermal and ectodermal tissues around the onset of neurulation, potentially enhancing long-range transmission of convergence forces. These results illuminate the mechanobiology of early vertebrate morphogenic mechanisms, aid interpretation of phenotypes, and give insight into the evolution of blastopore closure mechanisms.

Keywords: biomechanics, mechanobiology, force, gastrulation, convergent thickening, convergent extension, blastopore closure, Xenopus

INTRODUCTION

Major morphogenic (shape-generating) movements in the development of multicellular organisms occur by integration of local, force-generating activities and force-transmitting properties of individual cells into "morphogenic machines" that act across the tissue-level length scale. Understanding the physical aspects of tissue movements is essential for understanding how cells and gene products function in morphogenesis (Keller et al. 2003; Keller et al. 2008), and thus biomechanical measurements, mathematical modeling, and rigorous engineering standards play increasing roles in experimental analyses (see Jacobson and Gordon 1976; Hardin and Cheng 1986; Priess and Hirsh 1986; Hardin 1988; Hardin and Keller 1988; Koehl 1990; Hutson et al. 2003; Keller et al. 2008; Rodriguez-Diaz et al. 2008; Toyama et al. 2008; Layton et al. 2009; Varner et al. 2010). Semi-quantitative biomechanical properties of embryonic cells and tissues have been inferred from responses to micro-dissection (Beloussov 1990; Fernandez-Gonzalez et al. 2009; Ma et al. 2009; Solon et al. 2009; Martin et al. 2010; Fouchard et al. 2011), and in other cases, direct quantitative measurements have been made (Adams et al. 1990; Moore 1994; Davidson 1995; Davidson et al. 1995; Moore et al. 1995b; Davidson et al. 1999; Zhou et al. 2009; Zhou et al. 2010; Luu et al. 2011; David et al. 2014; Feroze et al. 2015). Here we link the generation of tensile force around the blastopore by tissues within the Involuting Marginal Zone (IMZ) to specific morphogenic machines operating during gastrulation and neurulation and provide a basis for testing the role of specific molecular components of these machines in generating tissue level forces.

Amphibian blastopore closure is thought to result from tensile convergence forces generated largely by the IMZ, an annulus of presumptive mesodermal tissue surrounding the blastopore (see IMZ, Fig. 1A). In our working model, as gastrulation begins, Convergent Thickening (CT,

white arrows, Fig.1A-B) of the IMZ decreases its circumference, which tends to push it toward and over the blastoporal lip, thereby contributing to involution of the mesodermal IMZ (black arrows, Fig. 1A, B). CT occurs in cultured giant sandwich explants over the same period (white arrows, Fig.1 C-D; Shook et al., in preparation). CT was originally defined in explants of the ventral IMZ of *Xenopus* as a convergence of tissue that drives radial (normal to the embryonic surface) thickening rather than the A-P extension that results from Convergent Extension (CE, see Keller and Danilchik 1988). As cells of the IMZ involute, they stop expressing CT and express *postinvolution behaviors*. The first cells to involute, those of the head, heart, lateroventral mesoderm (orange, Fig. 1A-B), migrate directionally across the blastocoel roof toward the animal pole (gray arrows, Fig. 1E). As cells of the later-involuting notochordal and somitic mesoderm (magenta and red, respectively, Fig. 1A) involute, they express mediolateral intercalation behavior (MIB), the polarized cell behavior that drives mediolateral cell intercalation, and thus CE (MIB- black, fusiform cells; CE- green and blue arrows, Fig. 1F). MIB (and thus CE) are expressed progressively, beginning anteriorly at the midgastrula (stage 10.5) with the formation of the Vegetal Alignment Zone (VAZ, Fig. 1E, E'). From this origin, MIB progresses posteriorly in embryos (Fig. F) and explants (Fig. G-H) (see Keller and Winklbauer 1992; Shih and Keller 1992a; Shih and Keller 1992b). In explants, MIB-driven cell intercalation shortens arcs of cells that extend to the explant margins and pulls the margins medially during CE (asterisks, Fig. J-K). In contrast, in embryos the ends are anchored at their junction with the vegetal endoderm in the region of bottle cell formation (asterisks, Fig. 1E', F, F'), and their shortening forms a tensile hoop just inside and beyond the point of involution (Fig. F), which drives constriction of the dorsal blastopore (Fig. 1C) and further CE of the dorsal tissues of the gastrocoel roof (GR, Fig. 1F'). The presumptive pattern of the future, post-involution MIB

mapped on the to IMZ of the embryo and giant explant (Fig. 1I and J, K, respectively) illustrate how A-P progression of MIB driven arc-shortening drives CE. This pattern of MIB expression was determined from time-lapse imaging of the progress of MIB across open-faced explants (Shih and Keller 1992b; Domingo and Keller 1995; Keller et al. 2000b). Congruent with the post-involution CE of the mesoderm, the overlying posterior neural tissue (spinal cord/hindbrain) also undergoes CE (dark blue, Fig. 1B), a CE that also occurs in explants without underlying mesoderm (Fig. 1G-H) (Elul et al. 1997; Davidson and Keller 1999; Elul and Keller 2000; Ezin et al. 2003; Ezin et al. 2006; Rolo et al. 2009; Ossipova et al. 2014). MIB occurs in various forms in ascidians (Munro and Odell 2002), fish (Jessen et al. 2002; Glickman et al. 2003; Lin et al. 2005), and in the mesoderm (Yen et al. 2009) and neural tissue (Williams et al. 2014) of the mouse.

Ventralized *Xenopus* embryos lack notochordal, somitic, and neural tissues and therefore do not express CE but nevertheless involute their IMZ and close their blastopores (Scharf and Gerhart 1980), suggesting that CT alone can close the blastopore (see Keller and Shook 2004) (Fig. 1L, M). IMZ explants from ventralized embryos show a rapid, near uniform CT throughout the IMZ (Fig. 1N-O). Some amphibians, such as *Gastrotheca rhiobambe* (del Pino 1996; del Pino et al. 2007) and *Eleutherodactylus coqui* (Shook, D., unpublished observations) close their blastopores solely or largely by CT and then express CE during the neurula stages (Shook, unpublished observations and see Keller and Shook 2004).

The role of these convergence-producing morphogenic machines in blastopore closure was inferred from the fact that breaking the continuity of the IMZ transverse to the axis of convergence results in catastrophic failure of normal involution and blastopore closure (Schechtman 1942; Keller 1981; Keller 1984; reviewed in Keller et al. 2003). Also, the force-

producing extension of dorsal IMZ explants (Moore 1994; Zhou et al. 2015) and the autonomous CE of "giant sandwich explants" (Poznanski et al. 1997) implies an active, force-producing convergence. Finally, disrupting MIB, which is thought to underlie CE, by perturbation of the planar cell polarity (PCP) pathway, blocks blastopore closure in embryos and blocks CE in sandwich explants and embryos (Djiane et al. 2000; Tada and Smith 2000; Wallingford et al. 2000; Habas et al. 2001; Goto and Keller 2002; Habas et al. 2003; Ewald et al. 2004). Zhou and others (2015) measured 'thickening' and extension force of dorsal isolates of the neurula, finding them nearly equal, and the blastopore lip of whole embryos can exert ~0.5 μN of force on cantilever probes (Feroze et al. 2015).

Here we use explants, including some or all of the IMZ, to assay the forces generated by tissues expressing the different morphogenic machines contributing to these forces, CT and CE, together or alone, using a mechanical measuring device (the "tractor pull" apparatus; See Methods) (Fig. 2). We show that the IMZ can generate and maintain large, constant, convergence forces and transmit them over long distances for long periods. We also use a uni-axial tensile stress-relaxation test (Wiebe and Brodland 2005; Benko and Brodland 2007) to show that the MZ and animal cap stiffe around the onset of neurulation. We also demonstrate a previously unknown transition in which CT generates most or all of the force to midgastrulation, at which time the IMZ progressively involutes, expresses MIB and contributes progressively more force. These methods provide a quantitative approach for evaluating the cellular and molecular mechanisms of developing convergence (tissue shortening) forces and tensile stiffness. Quantification of tensile convergence force and tensile stiffness offers new insights into the causes of failure of blastopore closure, body axis extension, and neural tube closure. Failures of these processes produce common, often linked, but poorly understood phenotypes, which result

from genetic and molecular lesions, notably of the PCP pathway (Ewald et al. 2004), and are of biomedical importance in neural tube defects.

RESULTS:

Giant Sandwich explants recapitulate most of the in vivo convergence movements of the IMZ

Time-lapse movies show that the mesodermal (IMZ) and neural (NIMZ) tissues in unencumbered (un-tensioned) giant sandwich explants undergo convergence similar to that seen in embryos, except that the rate peaked earlier in explants (Fig. S1A) and was only 57% of that in whole embryos during gastrulation (Table 1). Imaging explants as they were made revealed 600%/hr convergence in the first three minutes after cutting (Fig. S2), two orders of magnitude faster than that of post-construction explants or embryos (Table 1), suggesting that convergence against resisting tissues (e.g. the vegetal endoderm) resulted in stored elastic energy in the embryo, in line with prior findings (Beloussov et al. 1975; Beloussov 1990; Fung 1993). Therefore rapid, unmeasured convergence of the IMZ occurred when freed of this resistance at explantation. Unencumbered giants and intact embryos reached a minimal rate of convergence by 9 hours after the onset of gastrulation (G+9h) (Fig. S1), when involution is complete and convergence occurs only as CE of the involuted mesodermal tissues and overlying neural tissue. The dorsal tissues in giant sandwiches converged and extended well (Fig. S3), and tissue differentiation, assayed by markers for notochord and somitic mesoderm, was as expected from previous work (Fig. S7) (see Keller and Danilchik 1988; Poznanski et al. 1997).

Giant sandwich explants generate a consistent pattern of force during blastopore closure

Assays of standard giant sandwich explants (Fig. 2B), beginning between control stages 10.25(G+1hr) and 11.5(G+3.5h), showed a consistent pattern of circumblastoporal (mediolateral) tensile force increasing with time, in two major phases (Fig. 3A, blue line). In the first phase, beginning when the explant pulled the cleat against the probe (Fig. 2I), usually

within the first 3 to 30 minutes of the assay, force increased steadily to over 1 μN by the end of gastrulation in control embryos (stage 13, G+6h) and increased further by early neurulation (stage 14, G+7.5h) when it plateaued at about 2 μN (Fig. 3A, blue line). A second phase of force increase began 3 hours later (late neurula stage 18, G+10.5h) with most samples exhibiting a second plateau at about 4 to 5 μN by G+15 to 18 (Fig. 3A, blue line, S4AB). Probe #3 measurements are similar but higher early than those of probe #4 (Fig. 3, green line, S4AB) due to measurements that began earlier. Animal cap sandwiches, which do not normally converge or extend, showed no convergence force (Fig. 3A, brown line), thus ruling out healing and other artifacts. Probe drift and friction were accounted for (see Supplementary Methods, Fig. S5).

Immunohistochemical staining showed normal differentiation of somitic and notochordal tissues undergoing CE in mechanically loaded (encumbered) sandwiches (Fig. S7A-D). As in unencumbered sandwiches, tissues in each half of the sandwich were fused with their counterpart in the other half (see Keller and Danilchik 1988; Poznanski et al. 1997). Notochords were sometimes split posteriorly (Fig. S7C), perhaps related to retarded convergence compared to that of unencumbered giants (Fig. S1B, S3). Also the NIMZ, especially the non-neural portion, converged very little (Fig. S1B, S3; Movie 2, 4).

Contributions of the changing expression of CT and CE to convergence force.

CT GENERATES CONVERGENCE FORCE EARLY AND THROUGHOUT GASTRULATION.

Giant explant tissues express CT alone in early gastrula stages, followed by progressive transition to MIB/CE-expressing tissues. The progressive transition from CT to CE allows using giant, dorsal, ventral, and ventralized explants to ferret out the contributions of each morphogenic machine. The IMZ of unencumbered giant explants converges equally across its

mediolateral extent, without anisotropic (dorsally-biased) extension through G+2h (stage 10.5) (Movie 4). Thus CT is expressed early, from the onset of gastrulation, and everywhere in the IMZ, rather than just ventrally and later, as previously thought (Keller and Danilchik 1988). To measure early forces, giant explants were made from late blastulae (the dorsal side identified by "tipping and marking"; see Methods), mounted in the apparatus and measured before gastrulation began and prior to expression of MIB/CE. Tension appeared as early as stage 10 (Fig. 3A, light blue line), and rose to 0.3 μN of force prior to the onset of MIB, which occurs at G+2h (Shih and Keller 1992b; Lane and Keller 1997), demonstrating that early forces are generated solely by CT. Ventral 180° sandwich explants (Fig. 2D-E), which do not form dorsal tissues or express CE but do show CT, and the entire marginal zone of UV ventralized embryos (Fig. 2F-G), which do not have dorsal, CE expressing tissues (see below) converge equally across their mediolateral extent, without isotropic extension until reaching an equilibrium state of convergence and thickening (Movie 3). These ventral sandwich explants showed initial force increase similar to standard giant explants, and plateaued at about 2 μN, similar to standard giant explants, but neither exhibited the second phase of force production. These results show that forces equivalent to those generated by a combination of CE and CT in standard giants during gastrulation, can be generated by CT alone in ventral tissues and that CT continues to operate if not replaced by CE.

EXPLANTS EXPRESSING CE OVER A LARGER PROPORTION OF THEIR MEDIOLATERAL ASPECT HAVE A REDUCED OR NO PLATEAU.

Late giant explants, made as in Fig. 2A-C but at the midgastrula stage, and Dorsal 180 explants (Fig. 2A-C) show a more continuous increase of tensile force, with a moderate or no

decline in the rate of force increase (Fig. 3C and D, purple and magenta lines, respectively) during the plateau of normal giants, and they show a final plateau of 3.5 to 4 μN (G+14h; stage 21-22), a little lower and earlier than normal giant explants.. The more continuous rise in force produced by these explants is correlated with absent or reduced intervening ventral and lateral (ventrolateral) regions, allowing a more direct attachment of MIB/CE expressing tissue to the attachment strips, which suggests that the presence of ventrolateral (presumptive posterior) tissues accounts for the plateau.

THE PLATEAU IS LIKELY DUE TO STRAIN IN THE VENTROLATERAL TISSUES.

We measured uniform convergence (= negative strain) rates along the mediolateral axis of unencumbered giants (data not shown; see movie 4), whereas encumbered giants show 70% of the convergence of encumbered giants in the dorsal sectors expressing CE, but none in more ventrolateral sectors not yet expressing CE during the first phase of force increase (Table 1). Comparison of the rate of shear of the explant with respect to the attachment strips (the rate of convergence of the edges of the widest part of the IMZ minus the convergence of the sled toward the anchor (Supplementary Materials: Morphometrics)), showed that shear accounted for substantially more of explant convergence than did sled movement (Table 1). During the plateau, overall IMZ convergence dropped by 1.6%/hr for probe 3 while shear dropped by 1.2%/hr, such that it matched the remaining convergence of 2.5%/hr (Table 1). By region, the overall decline in convergence was explained by a 0.6%/hr increase in strain in ventrolateral tissues and a 0.2%/hr decline in convergence in dorsal tissues. Thus, the plateau is due primarily to the increased strain of the ventrolateral tissues; this could be explained either by a decline in stiffness, or by a decline or stall of force generation in this region. Also, the end of the plateau in giant explant assays is associated with significantly increased convergence of the

ventrolateral regions by 2.2%/hr and significantly decreased convergence by 1.5%/hr in dorsal regions (Table 1), suggesting an increase in stiffness or force generation in these regions.

Tension developed by explants represents a progressively increasing, instantaneous stall force

Forces generated by the cells within the tissue increase tension and drive convergence. Because the probe resists this convergence, tension across the explant increases over time. Tension increase is limited by the stall force of the motors involved (CT, CE) and by the yield strength of the tissues involved. We use "stall" here in the sense that cellular convergence can no longer proceed, e.g. because the tension across individual cells engaged in MIB is high enough that they can no longer pull themselves between each other; it is less clear what factor limits convergence by CT. Once the yield stress for a tissue (force/area) is reached, forces generated by CT and CE result in plastic deformation of that tissue, and convergence in one region is balanced by strain in another. Understanding the behavior of the explant requires an understanding of the biomechanically complex structure of the explant, and its dynamic changes over time. Also, it may be assumed that yield strength and stall force as they apply to the explant are not "all or nothing" effects; there are likely to be multiple structures with different rates of viscous flow leading to different rates of plastic deformation across a range of tensions. And because each cell is a motor, and is differently arranged within the tissue, they will reach their stall force at different over-all tensions across the explant.

We propose that initially (first 20-30 minutes) convergence proceeds rapidly until the stall force of the machine(s) is reached. At this point, force increase slows, advancing only as additional cells are recruited, either by the progression of MIB into more posterior tissues, or as

shear allows convergence to proceed such that more MIB expressing cells are acting in parallel (see Fig. 1F-G), increasing the "instantaneous" stall force for the current extent of morphogenesis. It less clear what effect convergence allowed by shear would have on an increase of the overall stall force of CT, but results from ventralized explants (Fig. 3D) suggest that they too increase stall force with convergence. This slower rate of force advance continues until the plateau, at which point the level of tension across the explant reaches the yield stress for the LV region, which results in its observed slight increase in strain rate, while CE continues to drive convergence in more dorsal tissues.

Our model above, that encumbered explants are increasing tensile force as they recruit more cells into MIB, predicts that applying additional exogenous tension to an explant should prevent further force generation by the explant until shear has allowed enough convergence such that the instantaneous stall force rises above the current level of tension. To test this, we applied additional tension to explants at various stages through the end of the plateau, by increasing the strain on them (Fig. S8, C-E). Explants (n = 9) generally showed an immediate 0.5 to 0.6 μN increase in tension, which decayed quickly over the next 15 to 30 minutes, then remained static until the explants projected rise in force prior to being strained reached their new, current level of tension (e.g. Fig. S8 A,B). In no case did tensioned explants produce higher final amounts, or rates of increase, of force. These results demonstrate that increased tension stalls force increase, as predicted, and that while the explant can sustain greater tension, increased tension alone does not trigger increased force production.

If the force developed by the explant at a given time does represent an instantaneous stall force, we expect that decreasing tension by decreasing strain should allow more rapid convergence until the system maximum is reached again. Reducing strain by moving the anchor

toward the probe (Fig. S8 H,I) enough to decrease tension on the explant by 1.2 to 1.4 μN resulted in an immediate observed relaxation across the explant of from 0.6 to 1.2 μN, with the remainder corresponding to the rapid recoil of elastic strain during anchor movement (< 1 second). After the initial, rapid elastic recoil, explants converged at a rate similar to unencumbered explants (about 10%/hr, see Table 1), until recovering their prior tension levels (e.g. Fig. S8 F,G). Recovery was consistently (n = 6) rapid (< 15 minutes) during the first phase of force increase, whereas it was consistently (n = 4) slower (30 minutes or more) during the major plateau or during DBC re-expansion. After recovery during the first phase of force increase, explants converged at rates more typical of encumbered explants (about 4%/hr, Table 1). This rapid recovery supports our model that explants under tension are at an instantaneous stall force, with consequently retarded convergence during all but their initial period of force increase. The slower recovery of the explants to normal levels of tension during the plateau is consistent with lower levels of stored elastic energy, across the explant as a whole at this time (Discussion).

We tested the idea that less force was being generated during the plateau phase, based on the premise that reduced force generation results in lower stored elastic energy, which is presumably continuously dissipated by long term viscous tissue flow, loss to heat, etc. While not quantitative, the immediate, rapid elastic recoil (tension released by anchor movement – observed tension drop; see Fig. S8 F-I), which occurs at a rate much higher than observed for normal explant convergence, suggesting it is not dependent on metabolic energy expenditure (Chen 1981), should provide a qualitative assessment of the relative amount of elastic energy stored. Both the fraction of tension released by anchor movement that was recovered during rapid recoil and the rate of that recoil were greater during the first phase of force increase

compared to the plateau phase. We compared the fraction of tension relaxation that was recovered within the first 5 seconds (fractional recoil = immediate elastic recoil/tension released by anchor movement; see Fig. S8 F-I), and the rate of recoil in the first 5 seconds (recoil rate = immediate recoil distance (as a percent of total mediolateral explant width)/time). We found that the fractional recoil was 41% (S.E. = +/- 5%, n = 6) during the first phase of force production, compared to 28% (S.E. = +/- 5%, n = 3) during the plateau. The recoil rate was 670%/hr (S.E. = +/- 90%/hr; n = 7) during the first phase of force increase (similar to the recoil rate of 600%/hr seen in explants freshly cut from intact early gastrulae), compared to 390%/hr (S.E. = +/- 32 %/hr; n = 3) during the plateau. These results show that during a tractor pull, explants, like the intact embryo, store considerable elastic strain-energy, more of which is recoverable during the first phase of force increase than during the subsequent plateau. This is consistent with the idea that ventrolateral tissues have reduced force accumulation during the plateau (Discussion). Alternatively, the rate of dissipation may increase during the plateau, e.g. because the tissue has reached its yield stress and is deforming plastically.

Structural stiffness increases in all tissues around the end of gastrulation.

Because we expect that variations of convergence and strain across CT-CE expressing tissue depend in part on the tissue's spring-like properties, we asked whether these properties vary. A true elastic modulus could not be measured because the tests are not isometric nor the tissue homogeneous (see Supplementary Materials). Instead we estimated tissue stiffness along the mediolateral axis of the explants with a uniaxial, tensile stress relaxation test (Fig. 4), and estimated sagittal sectional areas from fixed samples (Fig. 5A; see Supplementary Materials). Fixed samples of standard Giant and Dorsal 180° explants show similar increases in sagittal area

(Fig. 5A) due to progressive MIB-mediated intercalation (Figures 1E-F, G-H). Ventral 180° explants increase in sagittal area until about the time of the plateau, then remain stable, suggesting either that thickening has reached an equilibrium, or is developmentally programmed to stop.

From the time-dependent stress decay (Fig.4C, F), parameters for a network model of stress relaxation were estimated (Fig. 4E; see supplementary materials), including the residual structural stiffness and constant of spring stiffness for the explant at 180 seconds after strain application (Fig. 5), as well as instantaneous structural stiffness and viscosity (supplementary materials, Fig. S9). A standard 300 μm displacement from the probe produced an average 12% (range = 8 to 14%) strain of the mesodermal region between the sleds by 180 seconds, in giant explants initially at rest. The modulus estimated from structural stiffness's along the mediolateral axis of giant explants rose significantly from 14 Pa (Pascals) at late gastrulation (G+4.8h) to 21 Pa by mid neurulation (G+8.7h) ($p < 0.01$, paired t-test, n = 6 vs. 6) (Fig. 5B). After release from tension, explants recoil rapidly and typically returned to near their initial width within three minutes, with about 25% of the initially applied strain lost to permanent, or plastic, deformation, leaving them about 3% longer.

D180° and V180° sandwich explants also showed a trend of increasing stiffness from gastrula to neurula stages (Fig. 5B) with both showing an increase between stages 12 and 14 (G+4.3 and 7.6h) but showed no significant differences from each other at any stage. Presumptive ectodermal (AC) sandwiches strained an average of 24% over 180 seconds showed increased structural stiffness ($p < 0.01$, n = 5 vs. 3) from gastrula to neurula stages (Fig. 5B), but their stiffness is not significantly different from that of standard giants at either stage. By late

neurulation AC explants also showed plastic deformations of 25% of total strain. AC explants were substantially more plastic during gastrulation however, with about 65% of the total strain remaining as plastic deformation, suggesting a lesser ability to store elastic strain energy than during neurulation.

The modulus estimated from the structural stiffness is a bulk property of the tissue as a whole, and depends on the mechanical properties of individual tissues, their organization, and overall geometry, where the sectional area transverse to the mediolateral axis may differ substantially in size or composition along that axis of the explant. To understand how differential strain of relates to blastopore closure we measured spring stiffness for each explant type over time. Standard giants, D180°, V180° and AC explants all showed a trend of increasing spring stiffness between gastrula and neurula stages (Fig. 5C). Standard giants did not differ significantly between gastrula stages but increased significantly from stage to stage thereafter ($P < 0.01$, n's = 6 vs. 6; 6 vs. 3), doubling between G+4.8 and G+8.7. AC sandwich explants also increased significantly ($P < 0.05$, n = 3 vs. 3) between gastrula and neurula stages. Standard giants had significantly higher spring stiffness than AC sandwich explants by 5 to 6 fold at all stages ($p < 0.05$ during gastrulation, $p < 0.01$ during neurulation; n's = 3 vs. 3 to 6), indicating that ectodermal tissues contribute little to the ability of the IMZ to resist tension along the mediolateral axis during tractor pulls. D180° explants showed greater increases compared to V180° explants and standard giants, but were not significantly different at any stage. V180° explants were similar to standard giants until after mid-neurulation when their spring stiffness was moderately (37%) but significantly lower ($p < 0.01$, n = 2 vs. 3). The greater spring stiffness

of giants vs. ventral 180° explants by the end of neurulation is consistent with increased overall stiffness of giants as dorsal tissue differentiation progresses laterally.

DISCUSSION

The circumblastoporal tissues (IMZ/NIMZ) produce and maintain long-term, long range, consistent patterns of convergence force throughout early development.

Giant sandwich explants (IMZ+NIMZ) generate and maintain a consistent pattern of convergence force throughout gastrulation, neurulation, and into the tailbud stage. Correction for drift of the two probes of different stiffness's yielded similar force profiles, suggesting that our results are robust to different sources of error. Wound healing at the edges of the explants (Davidson et al. 2002) or a response to cell lysate from surgery (Joshi et al. 2010; Kim et al. 2014) could generate force, but AC explants, which are also cut and heal, do not generate significant tensile force, making this unlikely.

CT generates preinvolution, circumblastoporal tension throughout gastrulation.

Previously, post-involution CE was thought to generate the convergence force driving blastopore closure and the post-involution extension that elongates the body axis (Keller and Danilchik 1988; Moore et al. 1995b; Keller et al. 2000a). CT was described in the ventral sector of the *Xenopus* gastrula (Keller and Danilchik 1988) but its force contribution to gastrulation was unknown. Here, several results show that CT generates circumblastoporal tension early and throughout the IMZ. First, standard giant explants produce force early (Fig. 3A), before MIB and CE have begun (G+2h, stage10.5) (Shih and Keller 1992b; Lane and Keller 1997). Second, ventral 180° and ventralized giant explants that do not express CE also generate circumblastoporal force, which is likely due to their expression of CT. Third, unencumbered ventralized giants show uniform CT throughout the MZ (Supplementary Movie 3). Thus CT generates all the IMZ convergence prior to the onset of CE at the early midgastrula stage (stage

10.5, G+2h). Although force from ventral and ventralized explants levels off during the plateau period of standard giants, it persists and contributes to blastopore closure throughout gastrulation by decreasing the circumference of the IMZ and directing it to the point of involution. CT may continue into neurulation and function in the late involution of the ventrally located, posterior paraxial mesoderm (Keller and Tibbetts 1989; Wilson et al. 1989b). These findings explain how ventralized *Xenopus* embryos (Scharf and Gerhart 1980) and normal embryos of some amphibians such as *Gastrotheca riobambae* (del Pino 1996) close their blastopores in the absence of CE (Keller and Shook 2004; del Pino et al. 2007) and symmetrically, as are CT movements in normal *Xenopus* embryos. These results also establish CT as a morphogenic machine independent of CE, and raise the question of how widely it occurs and how it is integrated with other movements, in amphibians as well as other species, (see below).

The force profile reflects the transition from CT to CE.

CT is a pre-involution process, and as the cells of the early involuting presumptive head, heart, and lateroventral mesoderm involute, they undergo a transition from CT to a well-characterized directed migration across the blastocoel roof (Winklbauer and Nagel 1991; Davidson et al. 2006) (Fig. 1E). As the late involuting presumptive notochordal and somitic tissues involute, they undergo a transition from pre-involution CT to post-involution CE with the onset of the MIB that drives CE (Fig. 1F). What we have learned about CT here, and what we know about the pattern of expression of CE in explants and in the embryo (Keller and Danilchik 1988; Keller et al. 1989; Keller and Tibbetts 1989; Wilson et al. 1989a; Wilson and Keller 1991; Shih and Keller 1992a; Shih and Keller 1992b; Domingo and Keller 1995; Domingo and Keller 2000) account for some of the

features of the mediolateral tensile force profiles of the several types of "linearized" giant explants and lead to a better understanding of forces acting in vivo during blastopore closure.

We represent the capacity of CT and CE to generate and transmit tensile force in the explants as a linear array of motors and springs (light ones representing CT, darker ones CE/MIB, Fig. 6). We assume that mechanical properties within the IMZ are uniform before CE begins, based on the mediolaterally uniform convergence during CT (Fig. 6A-B), and that CT pulls directly on the sled-anchor system without shearing with respect to the sled-anchor system, and thus accounts for all the measured force up to G+2.5h (Fig. 6B', gray arrow, E, blue line). The timing of CT in explants argues that this force occurs in the pre-involution IMZ of the embryo (grey arrow, Fig. 6F), and its uniform dorsoventral expression accounts for the relatively uniform convergence around the early, pre-CE blastoporal lip (Keller and Danilchik 1988). At stage 10.5, cells begin to undergo a transition from CT to MIB (CE) as they involute, beginning in the presumptive anterior somitic mesoderm with formation of the Vegetal Alignment Zone (VAZ), and progressing medially and posteriorly (Shih and Keller 1992b). At this point the explant is heterogeneous, with a presumptive anterior region of MIB (CE) located centrally and a presumptive posterior region of CT (Fig. 6C-C') spread across the remainder of the IMZ. The central MIB region is initially linked to the sled and anchor strips only via the lateral, CT expressing regions of the explant, and remains so until MIB spreads further laterally, a process that is retarded in explants under tension. In this period of constant force increase from mid-gastrulation to the beginning of the plateau (~G+7.5h), CT and CE (MIB) in the explants act in series, with increasing expression of MIB, increasing cell intercalation, and an increasing sagittal/parasagittal area of MIB expressing cells, which all pull in parallel along the mediolateral axis (Shih and Keller 1992a; Domingo and Keller 1995). During the plateau (G+7.5 to 10.5h) the central region of CE (MIB) continues positive convergence whereas

the lateral regions show increased strain (negative convergence), suggesting that in explants the MIB/CE motor/spring combination generates greater tension than that of CT and exceeds the yield strength of the CT regions, accounting for the plateau (Fig. 6C', gray/black arrow, E). As the progression of the transition from CT to CE (MIB) reaches the sled/anchor apparatus at the end of the plateau (G+10.5h), the weaker CT regions are replaced by MIB/CE regions, the weaker link is removed, and the force rises again (Fig. 6C-D, C'-D', black arrow, E, green line). This interpretation is supported by the fact that dorsal explants, which have MIB directly connected to the sleds, show no plateau, and older explants, which express MIB across a greater mediolateral span of the marginal zone, have reduced force increase during the plateau period (Fig. 6E, pink and magenta lines). In the embryo, however, the stronger MIB/CE region does not act in direct series with an intervening, weaker CT region; instead MIB originates at the lateral boundary of the somitic mesoderm at its junction with the vegetal endoderm, and is anchored there (asterisks, Fig. 6G, H). Thus in the embryo, from its initiation in the VAZ, through its progressive expression posteriorly, MIB and the resulting CE act alone to shorten the breadth of post-involution mesoderm between the lateral anchorages (Fig. 1E',F,F'). The influence of the post-involution expansion of MIB expression posteriorly from its onset in the VAZ is reflected in the progressively more anisotropic blastopore closure from stage 10.5 onward, and in the dorsal region of the IMZ dominating closure, something that cannot be accounted for by the isotropic convergence of pre-involution CT.

Unlike the case of CT, the total force generated by CE (MIB) is under-estimated by our measurements, because CE results in extension of many of the cells expressing MIB away from the zone directly between the sleds, and these cells therefore pull on the sled/anchor system at an increasing angle (Fig. 6D). However, the same is true in the embryo, as progressively more of the

population of MIB expressing cells lie far anterior of the posterior progress zone of MIB at blastoporal lip (Keller 1984; Keller et al. 1989; Keller and Tibbetts 1989; Wilson et al. 1989a)(Fig. 6G, H), and thus the force measured with the giant explant may reasonably approximate that generated at the blastoporal lip through the end of gastrulation.

The convergence of the somitic mesoderm during late neurulation involves MIB but also columnarization (thickening) (see (Wilson et al. 1989a); (Keller et al. 1989)), which forms converging "somitic buttresses" that may contribute to folding neural plate (Schroeder 1971; Keller 1976). Our force measurements of convergence forces exerted by the intact embryo during this time are unquestionably a substantial underestimate (see also Estimates of Force/cell, below), both for the reasons listed above, and because embryos have assembled their mesoderm and neural tissues into laminar aligned structures that have undergone the full extent of normal convergence movements, in contrast to the retarded convergence of our explants.

Finally, when we explant tissue it expends its stored elastic energy as it converges rapidly, and consequently its subsequent convergence is slower than intact embryos and the additional force is measured. Observed force is further reduced by friction, perhaps by 0.2 μN, despite the slick agarose pad beneath the explant and by the glass beads beneath the sled. Therefore force measured here should moderately underestimate that generated at the instantaneous stall force or yield strength of the embryo, for a given extent of morphogenic progress.

Explant stiffness

Xenopus embryonic tissues stiffen about 2 fold along their mediolateral axis around the end of gastrulation, regardless of the tissue type, suggesting a systemic mechanism. Such increases may have many causes, such as increased ECM deposition (Davidson et al. 2004;

Skoglund et al. 2006), increased cell-cell adhesion, or stiffness of cytoskeletal architecture (Zhou et al. 2009). The high plasticity after strain of the ectodermal tissue during gastrulation is consistent with its response to strain during epiboly, when its area is increased by about 2 fold (Keller 1975; Chien et al. 2015). Whatever the causes, the increase in the stiffness of all the tissues at the end of gastrulation may cause decreased plasticity, as well as the resetting of pseudo-elasticity to a thinner epithelial set point (Luu et al. 2011). Previous estimates of AP compressive stiffness of dorsal isolates at stage 11.5 (about 14 Pascals, Moore et al. 1995a; Zhou et al. 2009), are very similar to ML tensile stiffness at stage 11.5 (G+3.5h) measured here (Fig. 3B), suggesting that the same mechanical elements may be resisting ML widening in both cases. In explants, the constant of spring stiffness for dorsal tissue continues to rise after early neurulation while that for ventral tissue does not (Fig. 5C), in part because the transverse sectional area of tissue between the attachment strips increases in the former but not in the later (Fig. 5A). More reliable measurements will be required to properly resolve the relative stiffness of ventrolateral or posterior tissues expressing CT compared to dorsal tissues expressing CE.

Accommodation to load and stall force

Some evidence suggests that tissues modulate their force production in response to changes in load. The mechanical properties of embryonic tissues from different clutches vary (von Dassow and Davidson 2009), yet gastrulation proceeds at roughly the same rate, suggesting that force production accommodates to the tissue properties encountered. Explants of dorsal tissues embedded in gels of increasing stiffness respond by producing more force (Zhou et al. 2015). Time-lapse recordings of blastopore closure show occasional decreases in rate, including

temporarily stalling out and then recovering rapidly, as if transient overloads of resistance were being overcome by increased force production (personal observation). However, in our experiments increasing tension did not result in greater convergence force, and instead, temporarily stalled force increase until further morphogenesis had occurred. We suggest that this is because our explants are already at their instantaneous stall force (see below).

Our results suggest that explanted tissue builds tension relatively rapidly when initially encumbered, until it reaches its stall force. Further force increase is then limited by the rate at which the number of cells expressing MIB increases and by their rate of intercalation, such that more pull in parallel, rather than in series. Intercalation is in turn limited by the roughly 4%/hr rate of convergence allowed by explant shear off the attachment strips, lateral strain, and, to a much smaller extent, probe movement. We predict that allowing more rapid convergence should allow force to rise more rapidly. It is not clear how force generation by CT would be expected to change as tissue thickens, but the ventral/ventralized tractor pulls show that force increase correlates with thickening, until both cease once reaching the plateau.

Mesodermal tissues in normal embryos are probably rarely at their stall force, since convergence occurs more rapidly. When convergence is impeded, tension comparable to that generated in tractor pulls accumulates around the blastopore during gastrulation (Feroze et al. 2015), suggesting these are also measures of force at their instantaneous stall force. A more accurate reflection of forces in the embryo might be obtained by looking at points along the force-velocity curve more closely resembling the situation in the embryo, e.g. by starting with about 0.2 μN of tension and moving the anchor strip toward the probe at 1 or 2%/hr.

Estimation of forces generated per cell and tensional stress of convergence

To estimate the force generated per engaged cell, we determined the average effective sagittal-sectional area (SSA) of the deep mesoderm, the cell population we expect is effective in bulk force production during the tractor pull (Table 2). We estimate that the mean mediolateral tensile force per cell rises during the first half of gastrulation and stabilizes by mid gastrulation at around 2.3 nN/cell, where it remains. These values assume negligible contribution from neural tissues and give equal weight to each cell within the effective SSA, although different proportions of cells may express CT, CE or no force generating behavior and may direct force mediolaterally more or less efficiently. We assume a constant cell size, although some cell division occurs in the somitic mesoderm during gastrulation and neurulation. The constant force per cell is consistent with the idea that increasing stage-specific maximal force generation is limited primarily by morphogenesis, as it increases the SSA. We also calculated tensional stress within the effective SSA (Table 2), which was roughly 4-fold lower than the mediolateral tensile stress estimated from extension forces exerted by dorsal tissues in a gel (Zhou et al. 2015), which is not surprising given that their measurements capture all of the force generated during late neurula stages in tissue that has undergone normal morphogenesis, compared to our which primarily capture forces generated around the blastopore, as described above.

CT to CE, a major morphogenic, regulatory, and evolutionary transition in the Amphibia

The temporal, spatial parameters of the CT to CE transition, and its biomechanical implications, represent a major morphogenic and regulatory transition. The force traces show that CT-generated forces occur early and throughout the IMZ prior to its involution, whereas CE, and its underlying cell behavior, MIB, are expressed after involution and progressively, with

increasing numbers of cells acting in parallel with time (Shih and Keller 1992b). This progressive CT to CE transition at involution in *Xenopus* (Fig. 1, 6) explains the dominance of the symmetric circumblastoporal forces of CT in the pre-involution region of the early gastrula, and the dominance of the asymmetric, CE forces in the post-involution region of *Xenopus* embryos beginning from the midgastrula stage (Keller and Danilchik 1988). At the other end of the spectrum of CT-CE transition, *Gastrotheca riobambae* delays all CE until neurulation and has a completely symmetrical blastopore closure, both externally and internally (del Pino 1996). Others, such as the direct developing *Eleutherodactylus coqui* and *Epipedobates tricolor*, show intermediate CT-CE transitions (D. Shook, personal observations). In ongoing work, we are testing the idea that the deployment of CT and CE varies with the egg size and the amount and distribution of yolk and the mechanical challenges changes in these parameters present to the morphogenic machines of gastrulation.

Conclusions

Our findings illustrate that CT is one of the morphogenic machines that contribute to blastopore closure, along with CE and Vegetal Rotation (Winklbauer and Schuerfeld 1999) and that CT is capable of closing the blastopore on its own in the absence of CE patterning, as in ventralized embryos, although CT clearly can not reliably close the blastopore in the presence of patterned but non-functional CE (Djiane et al. 2000; Tada and Smith 2000; Wallingford et al. 2000; Habas et al. 2001; Goto and Keller 2002; Habas et al. 2003; Ewald et al. 2004). Presumably, blocking CT while allowing CE to occur in an inappropriate context would also block blastopore closure. Normal blastopore closure is the result of the coordinated expression of this system of machines in an appropriately configured biomechanical context, and is thus a

problem in systems biology. Our demonstration of the role of CT in this system furthers our understanding and ability to study this system. Failure of amphibian blastopore closure is not a "non-specific phenotype", but result from a failure of some part of this system, which as we have shown here, can be teased apart biomechanically.

METHODS

Embryo culture, manipulation and explant construction

X. laevis embryos were obtained and cultured by standard methods (Kay and Peng 1991), staged according to Nieuwkoop and Faber (Nieuwkoop and Faber 1967), and cultured in 1/3X MBS (Modified Barth's Saline). For explants made before stage 10 the embryos were tipped and marked to identify the dorsal side (Sive et al. 2000). Standard "giant", Dorsal 180°, and Ventral 180° sandwich explants were made at stage 10 to 10.25 as described previously (Shook et al. 2004) (Fig. 2A-E; Fig. S2A) and cultured in Danilchik's for Amy (DFA) (Sater et al. 1993). Ventralized giant explants were made from ventralized embryos (see below) (Fig.2F-G) without reference to "dorsal" as these embryos are symmetrical about the blastopore (Scharf and Gerhart 1980)(supplementary Movie 1). "Unencumbered" explants were those without a load (e.g. unrestrained in the measuring apparatus, below). For explants made before bottle cells had formed, the vegetal endoderm was cut away from the circumblastoporal region just below the transition in cell size, above which most bottle cells will form (Keller 1981). Explants were staged by time elapsed from stage 10 control embryos, and when the dorsal bottle cells began to re-spread (stage 11) (Hardin and Keller 1988). Animal cap sandwiches were made from the ventral portion of the blastocoel roof of stage 10 embryos (not shown).

Ventralization of embryos.

De-jellied embryos were placed in dishes made of 15 mm transverse sections of 60 mm diameter PVC pipe with Saran wrap stretched across the bottom, irradiated 6 or 7 minutes from below at about 35 minutes post fertilization on a UV trans-illuminator (analytical setting (Fotodyne Inc. Model 3-3500) and left undisturbed for at least an hour to avoid accidentally

rotating and thus dorsalizing them (Black and Gerhart 1986). Embryos were also ventralized by injecting β-catenin morpholino vegetally into the first two blastomeres (Heasman et al. 2000). Embryos forming bottle cells asymmetrically or earlier than the majority of ventralized embryos were discarded as being insufficiently ventralized. Control, ventralized embryos were cultured to control stage 35-38 and scored for their DAI (Kao and Elinson 1988) or to control stage 28 and stained for dorsal markers (Supplementary Materials) to evaluate the effectiveness of ventralization.

Image analysis

Explant morphometrics (described in Supplementary Materials) were done with NIH Image 1.6 software (Wayne Rasband, National Institutes of Health; available at http://rsb.info.nih.gov/nih-image/), Object Image (Norbert Vischer, University of Amsterdam; available at http://simon.bio.uva.nl/Object-Image/object-image.html) or Image J (http://rsb.info.nih.gov/ij/).

"Tractor Pull" biomechanical measurement apparatus

Explants were attached to two polyester shim stock strips (Small Parts, Inc. cat. # SHSP-010), ~~both~~ 25 μm thick x 0.8 to 1.5 mm wide, and one, the "anchor, 4 to 8 mm long, and the other, "sled", 3 to 5 mm long (Fig. 2H). A cleat of shim stock (Small Parts, Inc. cat# SHSP-200), 500 μm thick x ~ 500 μm on a side, was glued to the sled with clear fingernail polish (Sally Hansen "Hard as Nails") (Fig. 2H). The anchor and sled were coated with fibronectin (Roche cat # 11 080 938 00, at 20 μg/ml, in 1/3X MBS for 30-60 minutes at 37°C) and inserted 0.5 to 1.0 mm (15-30% of the mediolateral extent of the explant) between the inner faces of the lateral ends of the sandwich to allow attachment (30-60 minutes) (Fig. 2H). The explant was placed over a window

of cover glass (#1.5) in a 100 mm culture dish, and the anchor was attached to the window with high vacuum silicone grease (Dow Corning, Inc.) (Fig. 2I). Using the stage controls, the cleat on the sled was moved adjacent to a calibrated optical fiber probe (40-50 mm by 120 μm, Mouser, Inc. stock 571-5020821) mounted on the end of an aluminum rod fixed to an XYZ micromanipulator attached to an IX70 Olympus inverted microscope. The spring constants of these cantilever probes were calibrated by measuring deflection upon hanging short lengths of wire of known length/mass on the probe. Tension on the explant was measured by probe deflection recorded in high-resolution movies from below the window (40x objective, Olympus IZ70) and its behavior recorded simultaneously by time-lapse imaging from above (Olympus stereoscope). Glass beads (106 μm diameter, Sigma Cat#G-4649) between the sled and the window and a 200 to 300 μm thick, 1% agarose bed between the explant and the window lowered friction (Fig. 2I). Probe drift and sled-substrate friction were characterized (Supplementary Materials).

Force Measurement Test

Mediolateral tensile force was measured as the explants pulled the cleat of the sled against the probe. In most cases, the probe was placed adjacent to the cleat such that both probe and explant were unloaded at the start of the experiment. In others, the explant was "pre-strained" about 25%, by moving the cleat against the probe, and then away from it, or the explant was left under a pre-tension. Measurements were made to tailbud stages (~20hr) when the probe deflection generally ceased to increase significantly. The cleat was then backed off from the probe to determine the resting position of the probe. Tension could be adjusted during a force

measurement by moving the anchor away from or toward the sled, to decrease or increase strain (as in Fig. 4 A-D).

Probe position was recorded every six minutes, and probe displacement was translated into force by the following:

$$F_{(t)} = D_{(t)} \cdot M \cdot K_P \qquad (1)$$

where D is displacement in pixels, M is the magnification scale in μm/pixel and K_P is the spring constant of the probe in μN/μm. Drift was determined from the unstressed position of the probe before and after the assay, the difference interpolated linearly over the duration of the test and subtracted from the probe movement. Means of force traces were plotted, with the mean of hourly intervals and the standard error of the hourly mean shown as error bars.

Structural Tensile Stiffness Measurement: Uniaxial Tensile Stress Relaxation Test

For estimates of stiffness (Wiebe and Brodland 2005), anchor-explant-sled preparations were mounted as for force tests, and strain was applied along their mediolateral (circumblastoporal) axis by moving the stage 300 μm (10-12% strain) over one to a few seconds. Relaxation was allowed for 5 minutes, the stage was withdrawn 400 μm from the probe, and any further shape change were recorded (recovery). Probe positions were recorded every 0.5 to 30 seconds, and the anchor-explant-sled assembly was imaged every 1-10 seconds. The stage position was determined by a calibrated Metamorph image processor. The strain imposed on the explant was based on the relative position of two points in the explant that lay above the medial edges of the attachment strips. The explants were tested periodically during gastrulation and neurulation with unstressed periods (> 1 hour) between tests.

We modeled the time (t) dependent structural stiffness (SS(t), Pascals) using the following viscoelastic spring and dashpot model (Findley et al. 1989; Moore et al. 1995b):

$$SS(t) = S_{inf} + S_{sp} \cdot e^{(-t/\tau)} \qquad (2)$$

where the parameters are S_{inf} or stiffness at infinite time (residual stiffness), S_{sp} or instantaneous stiffness, and τ, the relaxation time constant, representing the half life of stress-relaxation. ε, the coefficient of viscosity, is related to τ by:

$$\varepsilon = \tau \cdot S_{inf}$$

The model assumes that instantaneous stiffness is reduced by viscous flow or remodeling of intra- or inter-cellular structures, until a residual stiffness, representing stable elastic elements of intra- or inter-cellular structure, is reached. SS(t) was calculated using the cross-sectional area of the tissue, force measurement, and observed strain over time, and two analytical techniques were used to generate the parameters S_{inf}, S_{sp} and τ (supplementary materials). Alternatively, an explant "spring stiffness" constant (K_E) was also calculated (Supplementary Materials).

ACKNOWLEDGEMENTS

This work was supported by NIH grant NICHD R37 HD025594 MERIT AWARD.

COMPETING INTERESTS

None of the authors have competing interests.

REFERENCES

Adams, D. S., R. Keller and M. A. R. Koehl (1990). "The mechanics of notochord elongation, straightening and stiffening in the embryo of *Xenopus laevis*." Development **110**: 115-130.

Beloussov, L. V. (1990). "Mechanics of animal development." Riv Biol (THD) **83**(2-3): 303-322, 227-345.

Beloussov, L. V., J. G. Dorfman and V. G. Cherdantzev (1975). "Mechanical stresses and morphological patterns in amphibian embryos." J Embryol Exp Morphol **34**(3): 559-574.

Benko, R. and G. W. Brodland (2007). "Measurement of in vivo stress resultants in neurulation-stage amphibian embryos." Ann Biomed Eng **35**(4): 672-681. DOI.org/10.1007/s10439-006-9250-1

Black, S. D. and J. C. Gerhart (1986). "High-frequency twinning of Xenopus laevis embryos from eggs centrifuged before first cleavage." Developmental Biology **116**: 228-240.

Bolce, M. E., A. Hemmati-Brivanlou, P. D. Kushner and R. M. Harland (1992). "Ventral ectoderm of Xenopus forms neural tissue, including hindbrain, in response to activin." Development **115**(3): 681-688.

Chen, W. T. (1981). "Mechanism of retraction of the trailing edge during fibroblast movement." J Cell Biol **90**(1): 187-200.

Chien, Y. H., R. Keller, C. Kintner and D. R. Shook (2015). "Mechanical strain determines the axis of planar polarity in ciliated epithelia." Curr Biol **25**(21): 2774-2784. DOI.org/10.1016/j.cub.2015.09.015

David, R., O. Luu, E. W. Damm, J. W. Wen, M. Nagel and R. Winklbauer (2014). "Tissue cohesion and the mechanics of cell rearrangement." Development **141**(19): 3672-3682. DOI.org/10.1242/dev.104315

Davidson, L. A. (1995). Biomechanics of Sea Urchin Primary Invagination. Biophysics. Berkeley, University of California at Berkeley**:** 227.

Davidson, L. A., A. M. Ezin and R. Keller (2002). "Embryonic wound healing by apical contraction and ingression in Xenopus laevis." Cell Motil Cytoskeleton **53**(3): 163-176. DOI.org/10.1002/cm.10070

Davidson, L. A., R. Keller and D. W. Desimone (2004). "Assembly and remodeling of the fibrillar fibronectin extracellular matrix during gastrulation and neurulation in Xenopus laevis." Developmental Dynamics: An Official Publication Of The American Association Of Anatomists **231**(4): 888-895.

Davidson, L. A. and R. E. Keller (1999). "Neural tube closure in *Xenopus laevis* involves medial migration, directed protrusive activity, cell intercalation and convergent extension." Development **126**(20): 4547-4556.

Davidson, L. A., M. A. Koehl, R. Keller and G. F. Oster (1995). "How do sea urchins invaginate? Using biomechanics to distinguish between mechanisms of primary invagination." Development **121**(7): 2005-2018.

Davidson, L. A., M. Marsden, R. Keller and D. W. DeSimone (2006). "Integrin [alpha]5[beta]1 and Fibronectin Regulate Polarized Cell Protrusions Required for *Xenopus* Convergence and Extension." Current Biology **16**(9): 833-844.

Davidson, L. A., G. F. Oster, R. E. Keller and M. A. Koehl (1999). "Measurements of mechanical properties of the blastula wall reveal which hypothesized

mechanisms of primary invagination are physically plausible in the sea urchin Strongylocentrotus purpuratus." Developmental Biology (Orlando) **209**(2): 221-238.

del Pino, E. M. (1996). "The expression of brachyury (T) during gastrulation in the marsupial frog *Gastrotheca riobambae*." Developmental Biology **177**: 64-72.

del Pino, E. M., M. Venegas-Ferrin, A. Romero-Carvajal, P. Montenegro-Larrea, N. Saenz-Ponce, I. M. Moya, I. Alarcon, N. Sudou, S. Yamamoto and M. Taira (2007). "A comparative analysis of frog early development." Proc Natl Acad Sci U S A **104**(29): 11882-11888.

Djiane, A., J. Riou, M. Umbhauer, J. Boucaut and D. Shi (2000). "Role of frizzled 7 in the regulation of convergent extension movements during gastrulation in *Xenopus laevis*." Development **127**: 3091-3100.

Domingo, C. and R. Keller (1995). "Induction of notochord cell intercalation behavior and differentiation by progressive signals in the gastrula of *Xenopus laevis*." Development **121**(10): 3311-3321.

Domingo, C. and R. Keller (2000). "Cells remain competent to respond to mesoderm-inducing signals present during gastrulation in Xenopus laevis." Dev Biol **225**(1): 226-240. DOI.org/10.1006/dbio.2000.9769

Elul, T. and R. Keller (2000). "Monopolar protrusive activity: a new morphogenic cell behavior in the neural plate dependent on vertical interactions with the mesoderm in *Xenopus*." Developmental Biology **224**(1): 3-19.

Elul, T., M. A. R. Koehl and R. Keller (1997). "Cellular mechanism underlying neural convergent extension in *Xenopus laevis* embryos." Developmental Biology **191**: 243-258.

Ewald, A. J., S. M. Peyrot, J. M. Tyszka, S. E. Fraser and J. B. Wallingford (2004). "Regional requirements for Dishevelled signaling during *Xenopus* gastrulation: separable effects on blastopore closure, mesendoderm internalization and archenteron formation." Development (Cambridge, England) **131**(24): 6195-6209.

Ezin, A. M., P. Skoglund and R. Keller (2003). "The midline (notochord and notoplate) patterns the cell motility underlying convergence and extension of the Xenopus neural plate." Dev Biol **256**(1): 101-114.

Ezin, A. M., P. Skoglund and R. Keller (2006). "The presumptive floor plate (notoplate) induces behaviors associated with convergent extension in medial but not lateral neural plate cells of Xenopus." Developmental Biology **300**(2): 670-686.

Fernandez-Gonzalez, R., M. Simoes Sde, J. C. Roper, S. Eaton and J. A. Zallen (2009). "Myosin II dynamics are regulated by tension in intercalating cells." Dev Cell **17**(5): 736-743. DOI.org/10.1016/j.devcel.2009.09.003

Feroze, R., J. H. Shawky, M. von Dassow and L. A. Davidson (2015). "Mechanics of blastopore closure during amphibian gastrulation." Dev Biol **398**(1): 57-67. DOI.org/10.1016/j.ydbio.2014.11.011

Findley, W. N., J. S. Lai and K. Onaran (1989). Creep and relaxation of nonlinear viscoelastic materials. New York, Dover Publications, Inc.

Fouchard, J., D. Mitrossilis and A. Asnacios (2011). "Acto-myosin based response to stiffness and rigidity sensing." Cell Adh Migr **5**(1). DOI.org/10.4161/cam.5.1.13281

Fung, Y. C. (1993). Biomechanics : mechanical properties of living tissues. New York, Springer-Verlag.

Glickman, N. S., C. B. Kimmel, M. A. Jones and R. J. Adams (2003). "Shaping the zebrafish notochord." Development **130**(5): 873-887.

Goto, T. and R. Keller (2002). "The planar cell polarity gene strabismus regulates convergence and extension and neural fold closure in Xenopus." Dev Biol **247**(1): 165-181.

Habas, R., I. B. Dawid and X. He (2003). "Coactivation of Rac and Rho by Wnt/Frizzled signaling is required for vertebrate gastrulation." Genes & Development **17**(2): 295-309.

Habas, R., Y. Kato and X. He (2001). "Wnt/Frizzled activation of Rho regulates vertebrate gastrulation and requires a novel Formin homology protein Daam1." Cell **107**(7): 843-854.

Hardin, J. (1988). "The role of secondary mesenchyme cells during sea urchin gastrulation studied by laser ablation." Development **103**(2): 317-324.

Hardin, J. and R. Keller (1988). "The behaviour and function of bottle cells during gastrulation of *Xenopus laevis*." Development **103**(1): 211-230.

Hardin, J. D. and L. Y. Cheng (1986). "The Mechanisms and Mechanics of Archenteron Elongation during Sea-Urchin Gastrulation." Developmental Biology **115**(2): 490-501.

Heasman, J., M. Kofron and C. Wylie (2000). "Beta-catenin signaling activity dissected in the early *Xenopus* embryo: a novel antisense approach." Dev Biol **222**(1): 124-134.

Hutson, M. S., Y. Tokutake, M.-S. Chang, J. W. Bloor, S. Venakides, D. P. Kiehart and G. S. Edwards (2003). "Forces for morphogenesis investigated with laser microsurgery and quantitative modeling." Science **300**(5616): 145-149.

Jacobson, A. G. and R. Gordon (1976). "Changes in the shape of the developing vertebrate nervous system analyzed experimentally, mathematically and by computer simulation." J Exp Zool **197**(2): 191-246.

Jessen, J. R., J. Topczewski, S. Bingham, D. S. Sepich, F. Marlow, A. Chandrasekhar and L. Solnica-Krezel (2002). "Zebrafish trilobite identifies new roles for Strabismus in gastrulation and neuronal movements." Nat Cell Biol **4**(8): 610-615. DOI.org/10.1038/ncb828

Joshi, S. D., M. von Dassow and L. A. Davidson (2010). "Experimental control of excitable embryonic tissues: three stimuli induce rapid epithelial contraction." Exp Cell Res **316**(1): 103-114. DOI.org/10.1016/j.yexcr.2009.08.005

Kao, K. R. and R. P. Elinson (1988). "The entire mesodermal mantle behaves as Spemann organizer in dorsoanterior enhanced *Xenopus laevis* embryos." Developmental Biology **127**: 64-77.

Kay, B. K. and H. B. Peng (1991). Methods in Cell Biology. New York, Academic Press.

Keller, R., M. S. Cooper, M. Danilchik, P. Tibbetts and P. A. Wilson (1989). "Cell intercalation during notochord development in *Xenopus laevis*." J Exp Zool **251**(2): 134-154.

Keller, R. and M. Danilchik (1988). "Regional expression, pattern and timing of convergence and extension during gastrulation of Xenopus laevis." Development **103**(1): 193-209.

Keller, R., L. Davidson, A. Edlund, T. Elul, M. Ezin, D. Shook and P. Skoglund (2000a). "Mechanisms of convergence and extension by cell intercalation." Philos Trans R Soc Lond B Biol Sci **355**(1399): 897-922. DOI.org/10.1098/rstb.2000.0626

Keller, R., L. Davidson, A. Edlund, T. Elul, M. Ezin, D. Shook and P. Skoglund (2000b). "Mechanisms of convergence and extension by cell intercalation." Philosophical Transactions of the Royal Society of London Series B: Biological Sciences **355**(1399): 897-922.

Keller, R., L. A. Davidson and D. R. Shook (2003). "How we are shaped: The biomechanics of gastrulation." Differentiation **71**: 171–205.

Keller, R. and D. Shook (2004). Gastrulation in Amphibians. Gastrulation: From Cells to Embryo. C. D. Stern. Cold Spring Harbor, NY, Cold Spring Harbor Laboratory Press**:** 171-204.

Keller, R., D. Shook and P. Skoglund (2008). "The forces that shape embryos: physical aspects of convergent extension by cell intercalation." Phys Biol **5**(1): 15007.

Keller, R. and P. Tibbetts (1989). "Mediolateral cell intercalation in the dorsal, axial mesoderm of *Xenopus laevis*." Dev Biol **131**(2): 539-549.

Keller, R. and R. Winklbauer (1992). "Cellular basis of amphibian gastrulation." Current Topics in Developmental Biology **27**: 39-89.

Keller, R. E. (1975). "Vital dye mapping of the gastrula and neurula of Xenopus laevis. I. Prospective areas and morphogenetic movements of the superficial layer." Developmental Biology **42**(2): 222-241.

Keller, R. E. (1976). "Vital dye mapping of the gastrula and neurula of Xenopus laevis. II. Prospective areas and morphogenetic movements of the deep layer." Developmental Biology **51**(1): 118-137.

Keller, R. E. (1981). "An experimental analysis of the role of bottle cells and the deep marginal zone in gastrulation of *Xenopus laevis*." Journal of Experimental Zoology **216**(1): 81-101.

Keller, R. E. (1984). "The cellular basis of gastrulation in *Xenopus laevis*: active, postinvolution convergence and extension by mediolateral interdigitation." Amer. Zool. **24**: 589-603.

Kim, Y., M. Hazar, D. S. Vijayraghavan, J. Song, T. R. Jackson, S. D. Joshi, W. C. Messner, L. A. Davidson and P. R. LeDuc (2014). "Mechanochemical actuators of embryonic epithelial contractility." Proc Natl Acad Sci U S A **111**(40): 14366-14371. DOI.org/10.1073/pnas.1405209111

Kintner, C. R. and J. P. Brockes (1984). "Monoclonal antibodies identify blastemal cells derived from dedifferentiating muscle in newt limb." Nature **308**: 67-69.

Koehl, M. A. R. (1990). "Biomechanical approaches to morphogenesis." Seminars in Developmental Biology **1**: 367-378.

Kushner, P. D. (1984). "A Library of Monoclonal-Antibodies to Torpedo Cholinergic Synaptosomes." Journal of Neurochemistry **43**(3): 775-786.

Lane, M. C. and R. Keller (1997). "Microtubule disruption reveals that Spemann's organizer is subdivided into two domains by the vegetal alignment zone." Development **124**: 895-906.

Layton, A. T., Y. Toyama, G. Q. Yang, G. S. Edwards, D. P. Kiehart and S. Venakides (2009). "Drosophila morphogenesis: tissue force laws and the modeling of dorsal closure." Hfsp J **3**(6): 441-460. DOI.org/10.2976/1.3266062

Lin, F., D. S. Sepich, S. Chen, J. Topczewski, C. Yin, L. Solnica-Krezel and H. Hamm (2005). "Essential roles of G{alpha}12/13 signaling in distinct cell behaviors driving zebrafish convergence and extension gastrulation movements." J Cell Biol **169**(5): 777-787.

Luu, O., R. David, H. Ninomiya and R. Winklbauer (2011). "Large-scale mechanical properties of Xenopus embryonic epithelium." Proc Natl Acad Sci U S A **108**(10): 4000-4005. DOI.org/10.1073/pnas.1010331108

Ma, X., H. E. Lynch, P. C. Scully and M. S. Hutson (2009). "Probing embryonic tissue mechanics with laser hole drilling." Phys Biol **6**(3): 036004. DOI.org/10.1088/1478-3975/6/3/036004

Martin, A. C., M. Gelbart, R. Fernandez-Gonzalez, M. Kaschube and E. F. Wieschaus (2010). "Integration of contractile forces during tissue invagination." Journal of Cell Biology **188**(5): 735-749.

Moore, S. W. (1994). "A fiber optic system for measuring dynamic mechanical properties of embryonic tissues." IEEE Trans Biomed Eng **41**(1): 45-50.

Moore, S. W., R. E. Keller and M. A. Koehl (1995a). "The dorsal involuting marginal zone stiffens anisotropically during its convergent extension in the gastrula of Xenopus laevis." Development **121**(10): 3131-3140.

Moore, S. W., R. E. Keller and M. A. R. Koehl (1995b). "The dorsal involuting marginal zone stiffens anisotropically during its convergent extension in the gastrula of *Xenopus laevis*." Development **121**(10): 3131-3140.

Munro, E. M. and G. M. Odell (2002). "Polarized basolateral cell motility underlies invagination and convergent extension of the ascidian notochord." Development **129**(1): 13-24.

Nieuwkoop, P. D. and J. Faber (1967). Normal Table of *Xenopus laevis* (Daudin). Amsterdam:, North Holland Publishing Company.

Ossipova, O., K. Kim, B. B. Lake, K. Itoh, A. Ioannou and S. Y. Sokol (2014). "Role of Rab11 in planar cell polarity and apical constriction during vertebrate neural tube closure." Nat Commun **5**: 3734. DOI.org/10.1038/ncomms4734

Poznanski, A., S. Minsuk, D. Stathopoulos and R. Keller (1997). "Epithelial cell wedging and neural trough formation are induced planarly in *Xenopus*, without persistent vertical interactions with mesoderm." Developmental Biology **189**: 256-269.

Priess, J. R. and D. I. Hirsh (1986). "Caenorhabditis elegans morphogenesis: the role of the cytoskeleton in elongation of the embryo." Dev Biol **117**(1): 156-173.

Rodriguez-Diaz, A., Y. Toyama, D. L. Abravanel, J. M. Wiemann, A. R. Wells, U. S. Tulu, G. S. Edwards and D. P. Kiehart (2008). "Actomyosin purse strings: renewable

resources that make morphogenesis robust and resilient." Hfsp J **2**(4): 220-237. DOI.org/10.2976/1.2955565

Rolo, A., P. Skoglund and R. Keller (2009). "Morphogenetic movements driving neural tube closure in Xenopus require myosin IIB." Dev Biol **327**(2): 327-338.

Sater, A. K., R. A. Steinhardt and R. Keller (1993). "Induction of neuronal differentiation by planar signals in *Xenopus* embryos." Developmental Dynamics **197**: 268-280.

Scharf, S. R. and J. C. Gerhart (1980). "Determination of the dorsal-ventral axis in eggs of Xenopus laevis: complete rescue of uv-impaired eggs by oblique orientation before first cleavage." Dev Biol **79**(1): 181-198.

Schechtman, A. M. (1942). "The mechanism of amphibian gastrulation. I. Gastrulation-promoting interactions between various region of an anuran egg (Hyla regilla)." Univ. Calif. Publ. Zool. **51**: 1-39.

Schroeder, T. E. (1971). "Mechanisms of morphogenesis: the embryonic neural tube." International Journal of Neuroscience **2**(4): 183-197.

Sherrod, P. H. (1995). Nonlinear Regression Analysis Program (NLREG). Nashville, TN.

Shih, J. and R. Keller (1992a). "Cell motility driving mediolateral intercalation in explants of Xenopus laevis." Development **116**(4): 901-914.

Shih, J. and R. Keller (1992b). "Patterns of cell motility in the organizer and dorsal mesoderm of Xenopus laevis." Development **116**(4): 915-930.

Shook, D. R., C. Majer and R. Keller (2004). "Pattern and morphogenesis of presumptive superficial mesoderm in two closely related species, Xenopus laevis and Xenopus tropicalis." Developmental Biology **270**(1): 163-185.

Sive, H., R. Grainger and R. Harland (2000). Early development of *Xenopus laevis*: a laboratory manual. Cold Spring Harbor, NY, Cold Spring Harbor Laboratory Press.

Skoglund, P., B. Dzamba, C. R. Coffman, W. A. Harris and R. Keller (2006). "Xenopus fibrillin is expressed in the organizer and is the earliest component of matrix at the developing notochord-somite boundary." Dev Dyn **235**(7): 1974-1983.

Solon, J., A. Kaya-Copur, J. Colombelli and D. Brunner (2009). "Pulsed forces timed by a ratchet-like mechanism drive directed tissue movement during dorsal closure." Cell **137**(7): 1331-1342. DOI.org/10.1016/j.cell.2009.03.050

Tada, M. and J. C. Smith (2000). "Xwnt11 is a target of Xenopus Brachyury: regulation of gastrulation movements via Dishevelled, but not through the canonical Wnt pathway." Development **127**(10): 2227-2238.

Toyama, Y., X. G. Peralta, A. R. Wells, D. P. Kiehart and G. S. Edwards (2008). "Apoptotic force and tissue dynamics during Drosophila embryogenesis." Science **321**(5896): 1683-1686. DOI.org/10.1126/science.1157052

Varner, V. D., D. A. Voronov and L. A. Taber (2010). "Mechanics of head fold formation: investigating tissue-level forces during early development." Development **137**(22): 3801-3811. DOI.org/10.1242/dev.054387

von Dassow, M. and L. A. Davidson (2009). "Natural variation in embryo mechanics: gastrulation in Xenopus laevis is highly robust to variation in tissue stiffness." Dev Dyn **238**(1): 2-18.

Wallingford, J. B., B. A. Rowning, K. M. Vogeli, U. Rothbacher, S. E. Fraser and R. M. Harland (2000). "Dishevelled controls cell polarity during Xenopus gastrulation." Nature **405**(6782): 81-85.

Wiebe, C. and G. W. Brodland (2005). "Tensile properties of embryonic epithelia measured using a novel instrument." J Biomech **38**(10): 2087-2094.

Williams, M., W. Yen, X. Lu and A. Sutherland (2014). "Distinct apical and basolateral mechanisms drive planar cell polarity-dependent convergent extension of the mouse neural plate." Dev Cell **29**(1): 34-46. DOI.org/10.1016/j.devcel.2014.02.007

Wilson, P. and R. Keller (1991). "Cell rearrangement during gastrulation of Xenopus: direct observation of cultured explants." Development **112**(1): 289-300.

Wilson, P. A., G. Oster and R. Keller (1989a). "Cell rearrangement and segmentation in Xenopus: direct observation of cultured explants." Development **105**(1): 155-166.

Wilson, P. A., G. Oster and R. Keller (1989b). "Cell rearrangement and segmentation in *Xenopus*: Direct observation of cultured explants." Development **105**: 155-166.

Winklbauer, R. and M. Nagel (1991). "Directional mesoderm cell migration in the *Xenopus* gastrula." Developmental Biology **148**: 573-589.

Winklbauer, R. and M. Schuerfeld (1999). "Vegetal rotation, a new gastrulation movement involved in the internalization of the mesoderm and endoderm in Xenopus." Development **126**: 3703-3713.

Yen, W. W., M. Williams, A. Periasamy, M. Conaway, C. Burdsal, R. Keller, X. Lu and A. Sutherland (2009). "PTK7 is essential for polarized cell motility and

convergent extension during mouse gastrulation." Development **136**(12): 2039-2048.

Zhou, J., H. Y. Kim and L. A. Davidson (2009). "Actomyosin stiffens the vertebrate embryo during crucial stages of elongation and neural tube closure." Development **136**(4): 677-688.

Zhou, J., H. Y. Kim, J. H. Wang and L. A. Davidson (2010). "Macroscopic stiffening of embryonic tissues via microtubules, RhoGEF and the assembly of contractile bundles of actomyosin." Development **137**(16): 2785-2794. DOI.org/10.1242/dev.045997

Zhou, J., S. Pal, S. Maiti and L. A. Davidson (2015). "Force production and mechanical accommodation during convergent extension." Development **142**(4): 692-701. DOI.org/10.1242/dev.116533

TABLES

	Average Rate of Convergence (μm/min) (n)	Average Rate of Convergence (%/hr) (n) (SEM)	Strain of Dorsal tissue (%/hr) (n) (SEM)	Strain of LV tissue (%/hr) (n) (SEM)	Shear w.r.t. attachment strips (%/hr)
Intact embryo, LI, 2 to 7 hours	10 (2 to 7)	17.5 (2 to 7) (1.8)			
Giant explant, unencumbered, LI, 0 to 7 hours	5 (3 to 10)	10 (3 to 10) (1.5)			
Standard pull, probe 3 (2 to 7.5 h)		4.1 (4 to 5) (0.7)	-7.2 (6) (1.5)	1.1 (6) (1.5)	3.7
Standard pull, probe 3 (7.5 to 10.5 h)		2.5 (5) (0.8)	-7.0 (6) (2.1)	1.7 (6) (1.9)	2.5
Standard pull, probe 3 (10.5 to 15.5)		3.7 (5) (0.7)	-5.5 (6) (1.6)	-0.5 (6) (1.3)	3.2
Standard pull, probe 4 (2.5 to 7.5 h)		4.5 (2 to 4) (0.7)			3.1
Standard pull, probe 4 (7.5 to 10.5 h)		1.7 (4) (0.8)			1.7
Standard pull, probe 4 (10.5 to 16.5)		3.0 (4) (0.6)			2.1

Table 1. Convergence and strain. Negative strains indicate convergence

Time from onset of gastrulation (hours)	Force (μN (n, +/- SEM))	Effective SSA (mm^2 (n, +/- SEM))	Estimated Force/cell (nN)	Force per effective SSA (Pascals)
1	0.25 (3, 0.08)	0.12 (1, n/a)	1.3	2.1
2.1	0.31 (3, 0.09)	0.11 (4, 0.014)	1.7	2.8
2.9	0.49 (4, 0.16)	0.13 (4, 0.018)	2.3	3.8
4.3	0.94 (4, 0.04)	0.27 (3, 0.024)	2.2	3.5
6.5	1.6 (5, 0.11)	0.41 (3, 0.020)	2.5	3.9
11.8	2.6 (6, 0.19)	0.68 (3, 0.051)	2.4	3.8

Table 2. Estimates of force per cell and tensional stress within effective sagittal section area (SSA) (deep mesoderm only). Based on a mean cell sectional area of 625 nm^2.

FIGURE LEGENDS

Figure 1. Current view of morphogenic machines in the embryo and explants.

Diagrams show the onset and progress of expression of convergent thickening (CT, white arrows) and convergent extension (CE, green/blue arrows) in embryos (A-F) and in explants (C-H). Expression of CT begins throughout the pre-involution region of the involuting marginal zone (IMZ) at the onset of gastrulation (A), which results in its decreased circumference, thereby pushing the IMZ toward involution (black arrows, A); CT continues throughout gastrulation and is thought to drive blastopore closure (B). In explants, CT of the IMZ begins immediately on release from constraints of explantation (C-D). At the midgastrula stage (stage 10.5), mediolateral intercalation behavior (MIB) begins in the post-involution anterior mesoderm (E, surface view; E' enlarged cutaway of pre-involution IMZ). MIB originates laterally, in the region of the epithelial bottle cells (BCs, asterisks) and progresses medially to form an arc of intercalating cells, called the Vegetal Alignment Zone (VAZ, E'); MIB is expressed in the same pattern in explants (G). From this point on, MIB expression progresses posteriorly, generating CE, which constricts the blastopore and narrows the post-involution notochordal and somitic mesoderm (F) and the gastrocoel roof (GR, F') along the length of the axis in embryos. In explants MIB/CE pulls the unanchored lateral margin of the somitic mesoderm medially while extending and narrowing the somitic and notochordal mesoderm (G, H). CT feeds cells into the A-P progressive expression of MIB (H). The presumptive pattern of expression of MIB is shown mapped on to the IMZ of the embryo (I) and its progression mapped on to the explant (J-K).

In contrast, ventralized embryos lacking presumptive somitic, notochordal and neural tissue, and thus CE/MIB, express only CT, which closes the blastopore symmetrically (L-vegetal view; M-sectional view), and explants from such embryos show only CT (N-O). Presumptive tissues are indicated (orange- head, heart, lateroventral mesoderm; magenta-notochord; red- somitic mesoderm ; dark blue-posterior neural, hindbrain, spinal cord; light blue-forebrain; grey-epidermis; yellow- vegetal endoderm). Shading from dark to light, where used, indicates progressively more anterior (A) to posterior (P) position, respectively.

Figure. 2. Explant construction.

Giant sandwich explants are made by cutting early gastrula stage embryos mid-ventrally, then vegetally just below the lower edge of the IMZ, such that the bottle cells are included, then animally roughly 30° above the equator (dashed lines, A; see also Fig. S2). Two such explants are then recombined, inner face to inner face, to make a Giant Sandwich explant (B, H). Giant explants contain presumptive notochordal mesoderm (magenta), somitic mesoderm (red), posterior neural tissue (hindbrain-spinal cord), as well as presumptive brain (light blue), epidermis (grey), and migratory leading edge mesoderm (orange). Dorsal 180° explants are made the same way as standard giant explants, with the right and left quarters are cut off (C). Ventral 180° sandwich explants are similarly, except the IMZ is cut dorsally rather than ventrally (dashed lines, D). Ventralized giant explants are made from UV irradiated embryos, and thus they form no or vey limited dorsal tissues (F, G). For mechanical measurements with the tractor-pull apparatus, the two halves of the sandwich are apposed with their inner, deep

surfaces next to one another, with fibronectin coated plastic strips, one bearing a raised cleat, inserted at each end (H). The explant is allowed to heal and attach to the strips, and then positioned above a cover slip window in a culture chamber (I). The stationary "anchor" strip is attached to the window with silicone high vacuum grease (magenta), and the explant is placed over an agarose pad (green). The moveable "sled" strip rests on glass beads resting on a cover slip filler layer (blue). An XYZ positioner is used to move a calibrated optical fiber probe, mounted on an aluminum bar, near the cleat, and the imaging chamber, which rests on a motorized stage, is then moved such that the cleat is as close to the probe tip as possible without deflecting the probe.

Figure 3. Force vs. time traces for tractor pulls.

Mean force production over time is indicated (A-D; solid lines). Time is measured from the onset of gastrulation at stage 10, and the correspondence with developmental stage is shown (E). Hourly means are shown as symbols, with standard errors of the hourly means indicated. The onset of individual traces represents the time at which the sled was initially pulled against the probe, with the exception of the Animal Cap explants. All pulls were against probe #3, except "Standard Giants, probe #4" (green, A and D) and the "Ventralized Giants" and "Ventral 180s" (orange and yellow respectively, D). The force trace for Standard Giant explants vs. probe #3 (blue) is included for all graphs except where only probe #4 was used (D). Gaps in force traces represent points at which different numbers of explants are included in the mean force trace. Controls (A) included Standard Giant sandwich explants (vs. probe #3, dark blue, n = 2 up to 2 hours, n = 4 through 15 hours; vs. probe #4, green, n = 6 through 12 hours, n = 5 through 18

hours), Animal Cap sandwich explants (purple, n = 4 from 5 to 17 hours, 2 to 3 otherwise). Early and Late tractor pulls (B) include Early Giant explants (from stage 10; light blue, n = 3) and Late Giant explants (from stage 12.5 ; purple, n = 5). Dorsal tractor pulls (C) include Dorsal 180° explants (pink, n = 3). Ventral tractor pulls (D) include UV ventralized explants (orange, n = 3 at 4 hours, 4 from 5 to 7 hours, 5 from 8 to 9 hours and 4 from 10 to 20 hours), ventral 180° explants (yellow, n = 3 at 3 hours, 4 from 4 to 20 hours) and are compared to Standard Giant explants vs. probe #4.

Figure 4. Schema of movements and measures involved in stress-relaxation test.

Start position, with cleat adjacent to probe. Stage is moved 300 microns (A, red arrow) against probe, to impose stress, with resulting probe deflection (A, black arrow). The explant shows an instantaneous strain (B, green arrow), then exhibits viscoelastic decay, or "relaxation" over time (C, green arrows), reducing the deflection of the probe (B, black arrow), until tension equals residual stiffness (in practice, E_{180}). Finally, the stage is moved back 400 microns (C, red arrow), which de-stresses the explant and allows the probe to return to its starting position (C, black arrow). The explant shows elastic recovery (D, green arrows). (E) A model of the explant as a viscoelastic material, with springs representing instantaneous (E_{SP}) and residual (E_{180}) stiffness, and a dashpot representing the viscosity, with relaxation time (half-time of decay), tau (τ). In an example of a stress-relaxation test (F), the stage to which the fixed strip is anchored is moved (F, light blue line) to impose a stress, by pulling the cleat against the probe (as in A, B). This imposes a strain (F, yellow line) on the explant, and deflects the probe (F, dark blue line).

The movement of the sled (magenta) initially parallels that of the probe, until the stage is moved away from the probe (as in C, D) at about 300 seconds, at which point the explant shows elastic recovery of the imposed strain, pulling the sled with it.

In order to estimate E_{sp} and τ we used non-linear regression curve fitting of the stress relaxation phase (C).

Figure 5. Stress-relaxation tests.

The sagittal sectional area (SSA) for different kinds of unencumbered explants was determined at points throughout gastrulation and neurulation from confocal z-series of RDA labeled explants (A, inset; scale bar = 1 mm in intact giant, 0.5 mm for sagittal cross section (at yellow line in giant)). Standard giant (magenta squares) and Dorsal 180° sandwich explants (blue diamonds) show similar progressions of SSA; a regression on both (violet dashed regression line, 0.085 mm^2/hour * (hours after G0) + 0.24 mm^2) was used to estimate stage specific SSA for both kinds of explants in stress-relaxation tests. The increase in SSA for V180° explants tended to plateau by about 8 to 10 hours, so a first order polynomial regression (green dashed line, -0.0042 $mm^2/hour^2$ * (hours after G0)^2 + 0.085 mm^2/hour * (hours after G0) + 0.25 mm^2, or 0.68 mm^2 at 10 hours or later) was use to estimate the stage specific SSA for V180° explants in stress-relaxation tests. The SSA of animal cap explant sandwiches was a consistent 0.16 mm^2. Estimated SSA, measured force on the probe at 180 seconds, and measured proportional strain on the explant at 180 seconds were used to determine the stiffness (E_{180}) at several times during gastrulation and neurulation (B). Standard giant sandwich explants (dark green line), as well as

Dorsal 180° (light blue) and Ventral 180° (orange) sandwich explants and animal cap sandwich explants (Yellow) were tested. In order to compare the force-bearing capacity of different tissues, a bulk spring stiffness (Force at 180 s / Strain at 180 s) was plotted (C). Error bars = standard error of the mean, n's = 3 to 6, except where no error bar is shown, where n =1.

Figure 6. Model of how the convergence forces measured in the tractor pull are related to modules of cell behavior in explants and embryos.

Early convergence forces are generated largely by the CT machine (CT symbols, B-D). The CT symbol implies ML tensile force, represented by the inward pointing arrows, and radial compressive force, represented by the dot and indicating force directed in and out along the radial axis of the embryo (see 3D representation). As CE begins, MIB (fusiform, black cells) progressively replaces the CT machine from presumptive anterior to posterior (CE symbol: green convergence, blue extension arrows, C, D) while CT continues in more posterior tissues (CT symbol, C, D). At or shortly after the onset of mesdoermal MIB, MIB and CE begins in the posterior neural tissue (blue tissue, CE symbols, C, D).

Thus the IMZ tissues express a changing combination of CT and CE as development progresses. We represent CT and CE as modules, expressing distinctive spring constants (grey or black coils) and motor strengths (red and grey or black symbols), with the lighter spring and motor indicating CT and the darker CE (B'-C'). Initially, up to about G+2hr, the entire IMZ is comprised of CT-modules (B'), which represents the situation and generates the forces seen in the first two hours of early pulls (follow grey arrow from B' to E, blue line). These forces likely approximate force generated in the preinvolution (uninvoluted) IMZ of the whole embryo (follow the gray

arrow to F, CT symbols). As MIB begins, a CE module lies centrally, flanked by CT-modules in series (C') with lateral edges attached to the strips (C), which represents the situation and generates the forces measured from G+2 to 10.5h, including the period during the plateau in standard pulls (follow black/gray dashed arrows to E, green line), but with an increasing contribution from CE vs. CT modules after G+2h. As more cells express MIB, the number pulling in parallel increases, increasing the spring constant and motor strength of the CE module.

Because the VAZ forms as an arc it does not initially pull directly on the attachment strips (C; green arrows at edge) but on the intervening CT modules. The nascent CE module is initially small and weaker than the adjacent CT modules, but becomes larger over time, resulting in both increasing spring constant and motor strength. This eventually overpowers the shrinking CT modules, such that their convergence is reduced (C', more open coils), which dissipates some of the tension generated by the CE module, and thereby contributing to the plateau. In contrast, in the embryo, the CE (MIB) module is, from the beginning, always anchored to the endoderm at both ends, with only an indirect connection to CT modules in the lateral and ventral portion of the MZ (not shown in F; see H, G). Thus CT acts as a continuous but diminishing ring of converging tissue outside the blastopore, while CE-expressing tissue inside the blastopore, primarily in series with the relatively inert endodermal tissue, acts in parallel with this ring.

The transient decline rather than plateau in the rate of force increase during late pulls (E, magenta line) can be explained by a larger domain comprised of CE modules and smaller domains comprised of CT modules, compared to standard control pulls at the onset of the plateau, such that not all force generated by the CE domain was absorbed by reduced convergence in the CT domain. Once MIB progresses laterally to points of attachment with the

strips (D, D'), the decline ends; this represents the situation during the second phase of force increase (follow black arrow to E, magenta line and to H, G). At this point, all the force generated by CE and MIB in posterior tissues are transmitted to the attachment strips, while, with the progression of MIB posteriorly, force from more anterior tissues is transmitted progressively more indirectly, at an angle (green arrows; D). Dorsal pulls (E, pink line) show no plateau, because they contain little or no tissue comprised of CT modules (D') by the onset of the plateau (follow solid black arrow to E, pink line).

SUPPLEMENTARY MATERIALS

Supplementary methods, results and discussion:

Drift test:

Probes were placed in distilled water and imaged every 3 minutes. Force equivalents for the observed drift were calculated, for purposes of comparing different probes and the effect of drift on force measurements. Probe #3 showed minimal drift, within +/- 0.5μN over 6 hours (Fig. S5a). In most cases the most rapid drift occurred within the first 60 minutes. Probe #4 shows much more dramatic drift (Fig. S5b), especially when recorded from shortly after the dry probe was immersed (Fig. S5C). However, in nearly all cases, within 30 minutes of immersion probe #4 showed drift that was near linear over the range of forces we consider. When probe #4 was allowed to soak overnight, it had reduced probe drift (turquoise line that reaches 0.5μN, Fig. S5B). Drift for probe #4 may have to do with hydration and/or temperature equilibration of some element of the probe-holder assembly. By soaking the probes for 60 minutes prior to use and correcting for any remaining drift (as measured at the end of the tractor pull, upon the release of the explant from the probe) by interpolating over the period of force measurement, we minimized the error contributed by drift.

Friction test:

To evaluate the friction between the sled and the under-laying substrate, we moved the stage holding the tractor pull chamber such that the cleat on an unattached sled was

pushed against a stationary probe, recorded the probe position every 100-200 seconds and calculated the force exerted on the probe at each time for 2-6 hours. We compared the friction of the sled with the substrate, 1) on bare glass, 2) with an agarose pad of roughly 50-100% larger area under the sled and 3) with a sparse layer of 100μm glass beads under the sled. Tests were done in DFA, which contains 0.1% BSA. A representative example of test runs on different substrates is shown (Fig. S6). Treatment of the glass beforehand (e.g. by acid-ethanol wash and/or coating with BSA) appeared to have minimal effect. For glass, agarose and beads (n's = 4, 5 and 7), the average median forces were 0.41, 0.48 and 0.25 μN respectively. The average minimum forces were 0.27, 0.36 and 0.00 μN. The average standard deviation was 0.10, 0.07 and 0.14 μN. The force on the probe was below 0.32, 0.40, and 0.09 μN 10% of the time. And the fraction of the time forces were below 0.25 μN was 12, 23 and 64%. Although the 1.5 to 2-fold differences in the median friction force was only a moderate improvement, the difference in the time the friction force was at or near 0 μN on beads was dramatic. Rather than experiencing a fairly steady approximately 0.4 to 0.5 μN of friction in the case of glass or agarose, sleds over beads experienced lower friction much more frequently. For this reason, we used a sparse layer of beads in all force measurement and stress-relaxation tests. We assume that force measurements are approximately 0.2 μN below the force explants could produce at a given time.

Immunohistochemistry & Effectiveness of Ventralization.

For immunohistochemistry, embryos and explants were fixed at stage 26-28 in MEMFA (Kay and Peng 1991) overnight at 4°C and transferred to methanol for storage at –20°C.

Fluorescent staining for notochord with Tor-70 (Kushner 1984) and for somitic mesoderm with 12/101 (Kintner and Brockes 1984) was done as previously described (Bolce et al. 1992). Notochord and somites in giants from tractor pulls were generally elongated orthogonal to the mediolateral axis, although to a lesser extent than in an unencumbered giant. In standard giant or D180° sandwich explants from tractor pulls, the posterior ends of the two notochords frequently did not fuse, and in some cases most of the notochords were separate, but co-linear (Fig. S7 A-H). The two files of somites do fuse (Fig. S7 A-H). In tractor pull explants where an additional strain was imposed, both posterior notochord and somites often did not fuse, and sometimes elongate non-orthogonally to the axis of pull (Fig. S7 I-L); in a few cases, the two sets of notochords and somites remained largely independent, which tended to be coupled with generally aberrant morphogenesis.

UV ventralization for 5 to 7 minutes gave an average DAI of 1.8 (n = 318). Embryos of DAI score 0 to 3 generally manifested little or no evidence of CE prior to the end of neurulation, indicating that we had effectively eliminated CE in our embryos during the period of force measurement. Ventralized sandwich explants in some cases contain small amounts of somitic tissue, but rarely show any notochordal tissue (Fig. S7 M-P). Among unselected embryos, some notochord appeared infrequently (4%, n = 56) while some somite appeared more frequently (40%, n = 54). When ventralized giant sandwich explants did have some dorsal tissue, it generally didn't manifest (show any sign of CE) until after the plateau had been reached, and generally detracted rather than added to the force.

Morphometrics.

The sagittal sectional area of unconstrained giants sandwiches was determined from RDA-labeled explants (50 ng/embryo), cultured to control stages 10.5 to 19, fixed in MEMFA and imaged in the laser scanning confocal. Minimal changes in explant dimensions were seen after fixation (< 5%, n = 6). The Z-step distance of the confocal was calibrated using a coverslip fragment of known thickness immersed in a solution of RDA. En face confocal images for the entire explant were obtained, re-sliced to show the mid-sagittal sectional plane, and the area of these plotted against stage. A regression was plotted on the sagittal sectional area (SSA) of several explants, and this was used to estimate the sagittal sectional area of the explants used in the stress-relaxation test. To estimate the effective SSA, explants were sliced parasagittally and parasagittal confocal images were collected, from which the area of the deep mesoderm was estimated, constrained by cell size and distance from the bottle cells.

Proportional convergence or strain along the mediolateral axis for defined regions of explants was calculated by measuring the distance (L) between specific cells or distinctively pigmented regions within the explant initially ($L_{(i)}$) and at time t ($L_{(t)}$), to give time specific strain:

$$S_{(t)} = (L_{(t)}-L_{(i)})/L_{(i)}$$

Rates were then $S_{(t)}/\Delta t$. Convergence is expressed as strain * -1.

Convergence in giant sandwiches were with respect to the mediolateral extent of the limit of involution at the onset of time-lapse recording ($L_{(i)}$) and thereafter. Rates of

convergence during giant construction were instead with respect to the initial circumference in the intact embryo.

Shear rate of explant with respect to attachment strips for a given time period was calculated as:

$$\text{Shear rate} = (\Delta W - \Delta D)/W(i)/\Delta t * 100\%$$

where W(i) is the initial width of the widest part of the mesendoderm at the onset of the assay, ΔW is the change in width during the time period, ΔD is the displacement of the sled strip toward the anchor strip during the time period and Δt is the elapsed time.

Estimation of parameters for Spring and Dashpot Model:

Two alternative methods were used to determine parameters for the spring and dashpot model

$$SS_{(t)} = SS_{INF} + SS_{SP} * e^{(-t/\tau)} \qquad (2, \text{from main text})$$

based on the observed time (t, in seconds) dependent structural stiffness (SS), calculated as:

$$SS_{(t)} = F_{(t)} / (SSA \bullet S_{(t)}) \qquad (3)$$

where time specific force ($F_{(t)}$) was as calculated in eq. 1 (main text), SSA was the estimated stage specific sagittal sectional area (see Morphometrics, above), and $S_{(t)}$ the

time specific strain (see Morphometrics, above) was measured from the mediolateral extent of the mesodermal component of the explant spanning the gap between the strips to which they were attached.

In the first method ("log transform"), SS_{INF} is assumed to be 0.97 * $SS_{(180)}$ because stress decay has stabilized by 180 seconds, and active convergence is likely to overwhelm further relaxation. Given eq. 2, a linear regression on

$$y(t) = \ln(SS_{(t)}-SS_{INF})$$

then yields the line

$$y(t) = (-1/\tau) * t + \ln(SS_{SP})$$

and $SS_{INF} / SS_{(180)} = \sim 0.97$

In the second method, a curve-fitting program (NLREG, available at http://www.nlreg.com, Sherrod 1995) was used to generate the parameters SS_{INF}, SS_{SP} and τ. In both cases, viscosity (η) is determined as:

$$\eta = SS_{SP} * \tau$$

Viscosity and instantaneous stiffness derived using the log transform method both show a significant increase between late gastrulation and mid-neurulation (Fig. S9 A,B, green), whereas using NLREG, they show no significant difference (Fig. S9 A,B, orange).

These viscosity estimates are roughly an order of magnitude lower than those measured by David et al. (David et al. 2014) on deep tissue alone. The major difference in the current study is that explants are deep tissue enclosed in superficial epithelium, which should lower the tissue surface tension.

The log transform method tends to match the later part of the stress-relaxation curve, giving a lower instantaneous stiffness and higher viscosity, whereas the reverse is true of the NLREG method (Fig. S10). The two methods highlight the fact that viscosity appears to be much lower during the first 10-15 seconds of stress relaxations than thereafter. This may reflect a change in the cellular elements that are viscously flowing over time, with very low viscosity elements flowing first, followed by successively higher viscosity elements. Because tissues in the embryo are already tension bearing, the viscosity derived form log regression more accurately reflects the relevant mechanical properties over developmental time scales.

An explant "spring stiffness" constant (K_E) was also calculated:

$$K_E = F_{(180)} / (L_{(180)} - L_{(0)})$$

with $F_{(t)}$ and $L_{(t)}$ as described above.

Caveats to stiffness measures of explants.

Our stiffness measurements represent an approximation of composite structural stiffness, rather than the true stiffness of a uniform material. Giant sandwich explants are

not homogeneous in any dimension, and after stage 10.5 (G+2h), the shape of the sagittal sectional area (SSA) begins to vary along the mediolateral extent of giant sandwich explants (Fig. S3; Movie 2). As a consequence, stiffness measures are biased toward the least stiff region along the mediolateral axis. In D180 and V180 explants at later stages, the mesodermal tissue rounded up to some extent, with a relatively circular cross section across the AP axis, with the attachment strips inserted part way into the circle. Stretch resulted in both over-all strain of the mesodermal tissue, but also flattening of the circular cross section. Probably as a consequence, later stiffness measurements from D180° explants in particular are more variable (Fig. 5C). We found that straining these rounded tissues 600 rather than 300 microns gave more consistent results for stiffness measurements, and so those results are reported.

Supplementary Discussion:

The nature of convergence by MIB may offer an alternative or complementary explanation as to why an increase in compressive load results in increased force whereas an increase in tensile load does not. The cell intercalation process is self-reinforcing in that it increases the number of units in the parallel, pulling array, but depends on the generation of additional tension in order for cells to pull themselves in between one-another. Thus some threshold of unresolved tensile load may retard further convergence via intercalation and thus limit additional force production, whereas an increased compressive load driving extension, the output of convergence, may activate compression-sensitive accommodation mechanisms while not immediately limiting the progress of intercalation. The differences in responses to compressive and tensile loads should be evaluated further.

SUPPLEMENTARY FIGURES

Figure S1. Comparison of convergence along the limit of involution (LI).

(A) The rates of convergence along the circumference or mediolateral extent of the LI in whole embryos, unencumbered giants and giants in tractor pulls under probe #3 or 4. (B) The extent of convergence at the limit of involution by G+7.5h of giant sandwich explants is retarded in the tractor pull (right), compared to an unencumbered giant (left). Red lines indicate the position of the strips.

Figure S2. Convergence during explant construction.

Embryos rapidly contract along their circumferential axis upon being cut. An example is shown (A), tracing the length of the equatorial (yellow) and sub-equatorial (cyan) circumference of the embryo, corresponding roughly to the limit of involution and the middle of the marginal zone. Stills are shown immediately before (0') and one minute after the embryo is initially cut (1', arrow head), after the removal of further vegetal endoderm at two minutes (2') and after flattening (3'), in preparation to construct a giant sandwich. Scale bar = 1mm. Comparing the circumferential lengths to that immediately prior to cutting (B) shows a rapid contraction along the mediolateral (former circumferential) axis. The explant in A was combined with another such explant to make a giant sandwich and gently pressed together under a coverglass to heal.

Figure S3. Comparison of morphogenesis in embryos, giants and tractor pulls.

Intact embryos (top) are compared to unencumbered giants (middle) and standard giants in tractor pulls (bottom). Time of controls are as indicated at bottom. Scale for embryos = 250 μm, for giants and tractor pulls = 1 mm.

Figure S4. Plots of all the individual force traces.

For each tractor pull condition, the force traces of each pull are plotted (thin lines), as well as the mean of the pulls (thick line), with error bars representing standard error. The accuracy of the plots along the time axis is approximately +/- 30 minutes. For Late Giants, UV Giant Pulls and Ventral 180° pulls, plots using both 3 and 4 are shown, as no significant difference was seen between the two probes for these conditions.

Figure S5. **Probe drift tests.**

Probe drift over time was assayed with the probe immersed in culture media or water. Probe movement was translated into force equivalents, to determine how much it would influence tractor pull and stress-relaxation test measurements. Representative plots with probe #3 (A) showed substantially less tendency to drift than with probe #4 (B, C). Drift was greatest immediately after immersion (C).

Figure S6. Sled friction tests.

Representative force plots for sled friction on three different substrates: cover glass in a 0.1% solution of BSA, a 1% agarose pad, or 100 μm glass beads.

Figure S7. Notochordal and somitic tissue in tractor pull explants.

Sandwich explants used in tractor pulls were fixed after the force measurement assay was finished (stage 25-30) (A, E, I, M) and stained for somitic tissue with the 12/101 antibody (B, F, J, N) and for notochordal tissue with the Tor70 antibody (C, G, K, O). The two staining patterns are also shown juxtaposed D, H, L, P). In a standard giant explant (A-D), a dorsal 180° explant (E-H) and a standard giant explant that had additional tension imposed on it (0.6μN, at G+5h) (I-L), both somitic and notochordal staining are evident. In a ventral 180° explant, (D-F) a small amount of somitic tissue at the lateral edge of the explant is observed, but no notochordal tissue. Tor70 signal in O is typical of that seen in the remnant of the blastocoel cavity of ventralized embryos with no axial tissues, and does not correspond to notochordal tissue. Scale bars = 1mm.

Figure S8. Response of explants in tractor pull after tension increase or relaxation.

The anchor strip was moved 50 μm away from the probe to increase tension on the explant by 0.5 to 0.6 μN (A, B). Two examples (green and red in A, B) are compared to mean control values (blue in A, B).

The anchor strip was moved 100 μm toward the probe to relax tension on the explant by 0.7 μN (F,G). In all cases, the point of maximum deflection is indicated by *. Two examples (blue and red in F, G) are compared to mean control values (green in F, G). Close-ups of the time period around the tension adjustment are shown in B, G.

Tension increase via anchor movement (red arrow; C), resulted in an immediate increase in the deflection of the probe (black arrow; C); as the explant underwent stress-relaxation (double headed green arrow; D), tension was reduced (green arrow; D). Eventually, continued convergence (double headed blue arrow; E) added additional tension to the system (blue arrow; E).

Tension reduction via anchor movement (red arrow; H), resulted in an immediate decrease in the deflection of the probe (red arrow; I); rapid elastic recoil (< 5 seconds) of the explant as stored elastic energy was released resulted in convergence of the explant (double headed blue arrow; I), and increased deflection of the probe (blue arrow, I). Further morphogenic convergence of the explant occurred subsequently (as in E).

Figure S9. Instantaneous Structural Stiffness and Viscosity of standard giant sandwich explants. Parameters for the spring and dashpot model (Fig. 4E), calculated using two different methods (NLREG or Log Transform).

Figure S10. Comparison of methods for estimating parameters.

(A) Example of estimation of parameters from linear regression on log transform of time-dependent stiffness data. Magenta: plot of ln(SS(t) - SS(180) * 0.97)). Black: linear regression plot on log transformed data. Blue: plot of ln(SS(sp) * e(-t/tau)), with parameter as estimated by NLREG.

(B) Comparison of Model vs. Measured Stiffness for the case in A, above. Blue: measured time dependent structural stiffness. Magenta: plot of E(180) + SS(sp) * $e^{(-t/tau)}$, with the later two parameters based on linear regression on log transform, as in A, above. Green: plot with all parameters from NLREG.

SUPPLEMENTARY MOVIES:

Supplementary Movie 1. Movie comparing regular (left) to ventralized (right) BP closure.

Supplementary Movie 2. Movie showing standard giant in tractor pull apparatus.

Supplementary Movie 3. Movie showing ventralized giant sandwich explant

Supplementary Movie 4. Movie showing unencumbered giant sandwich explant.

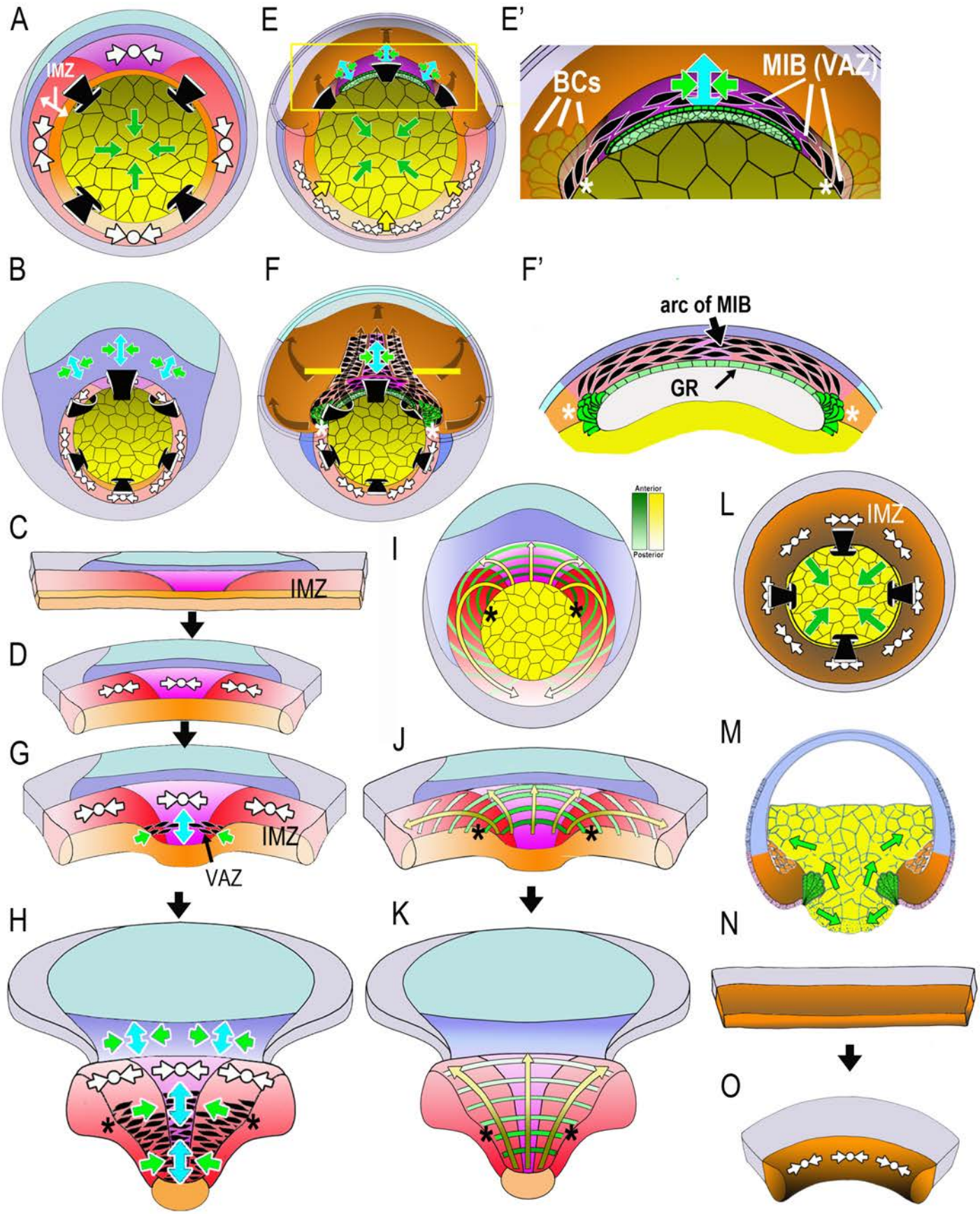

Figure 1 Shook et al.

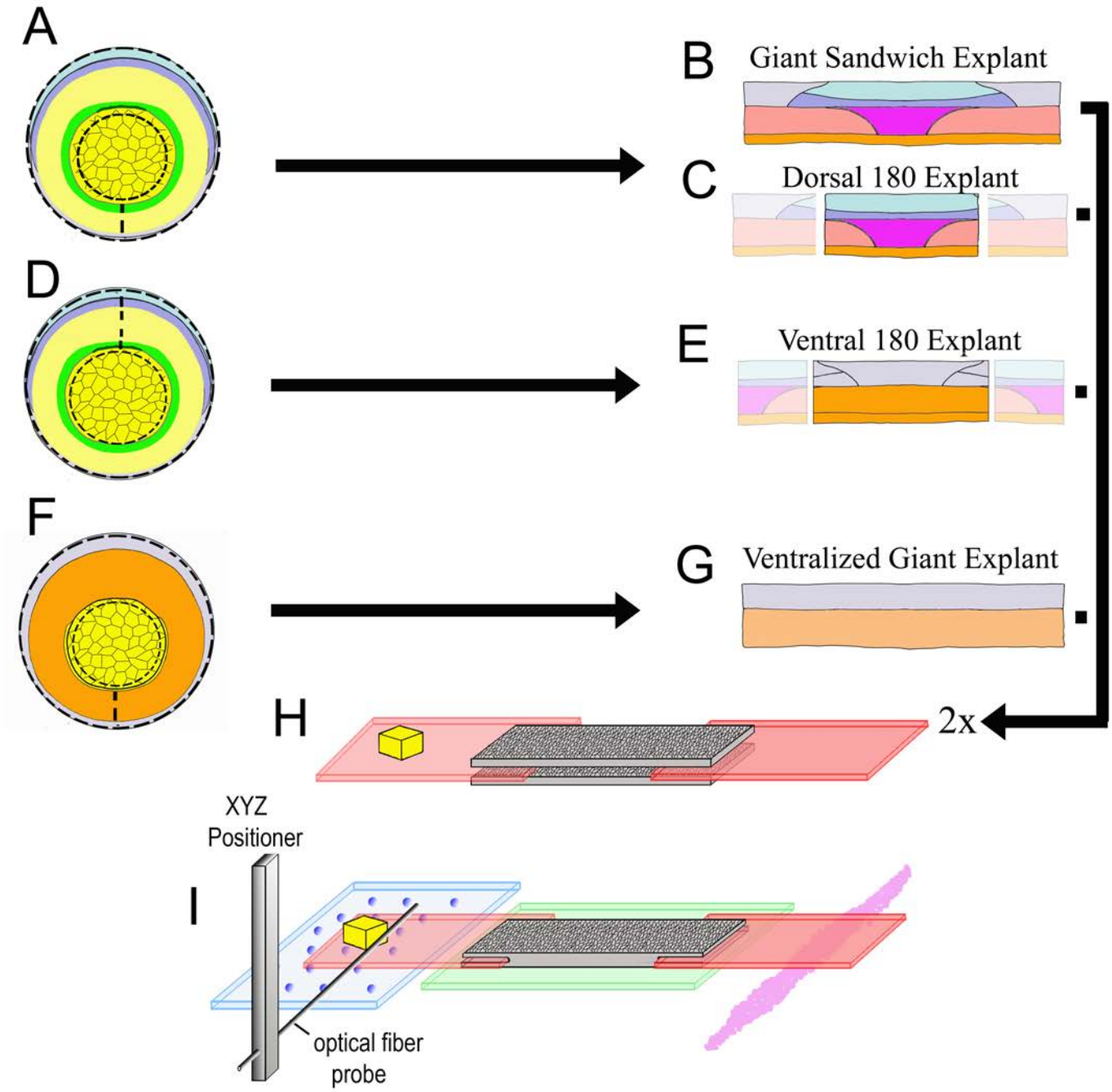

Figure 2

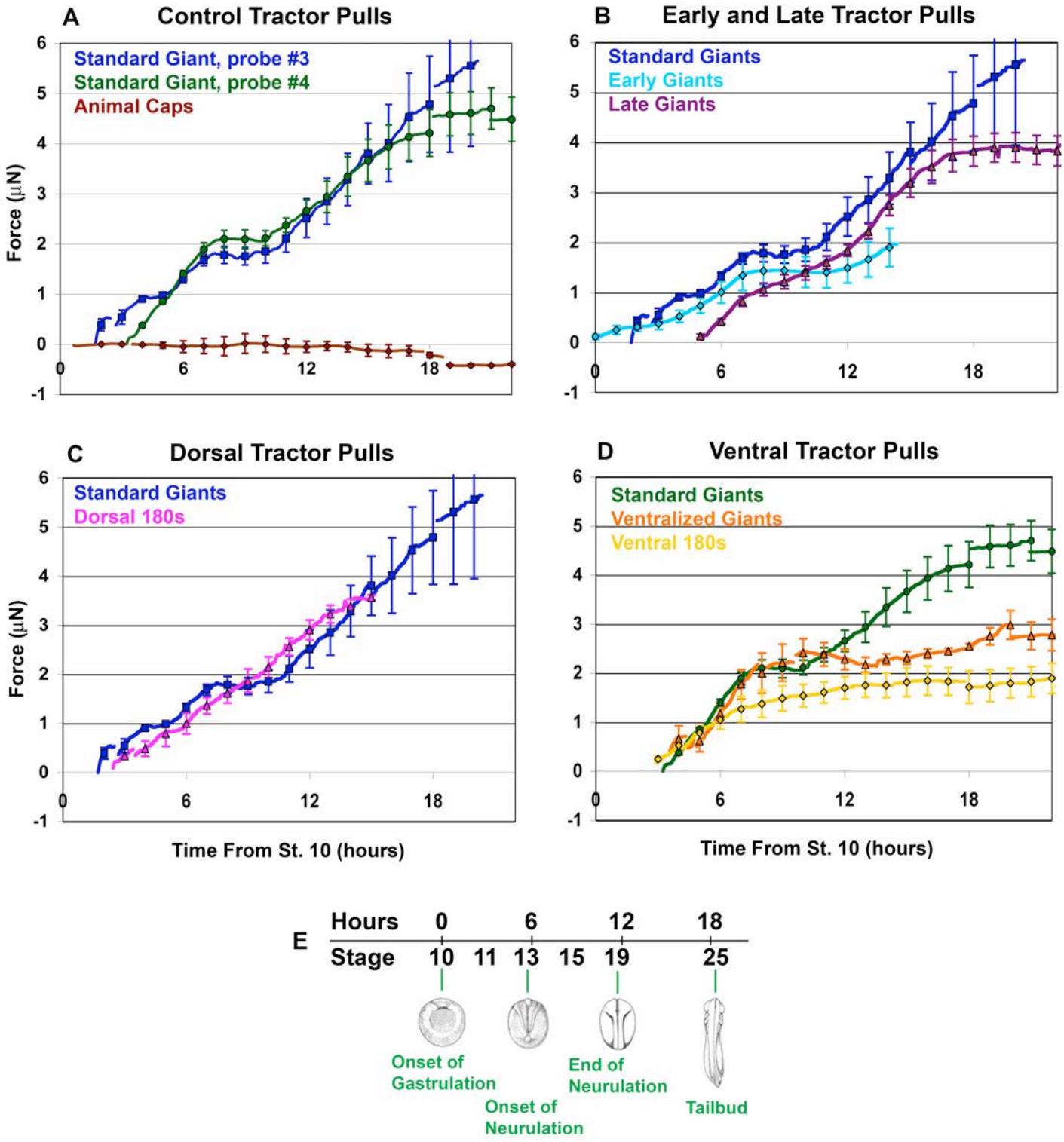

Figure 3

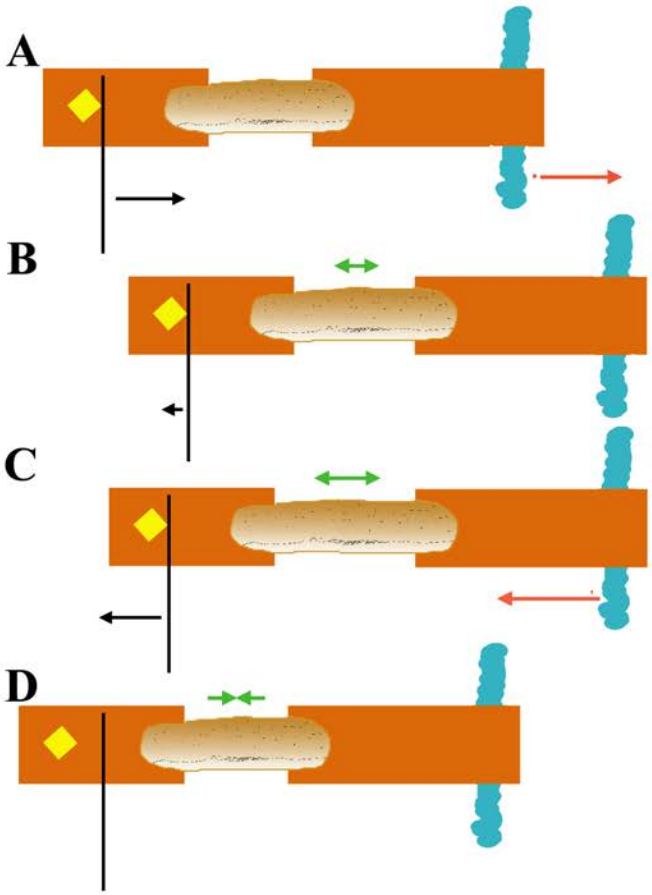

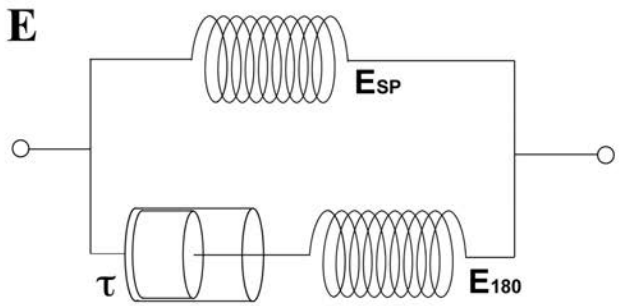

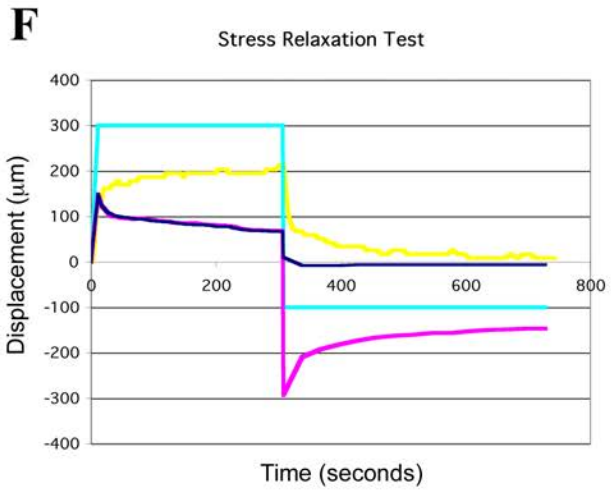

Figure 4

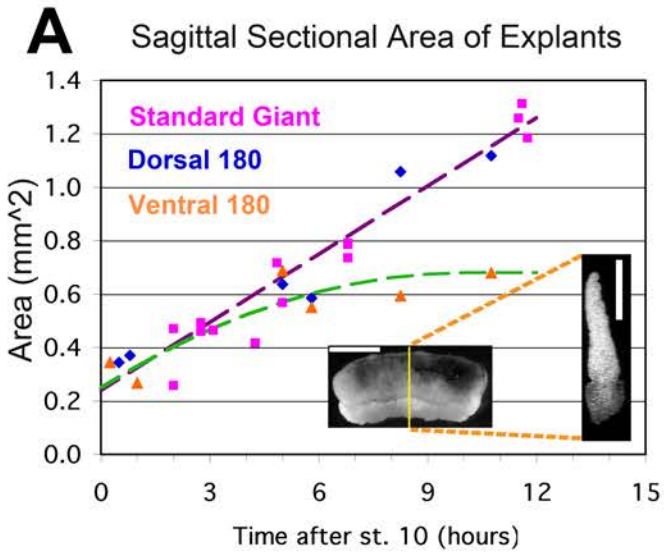

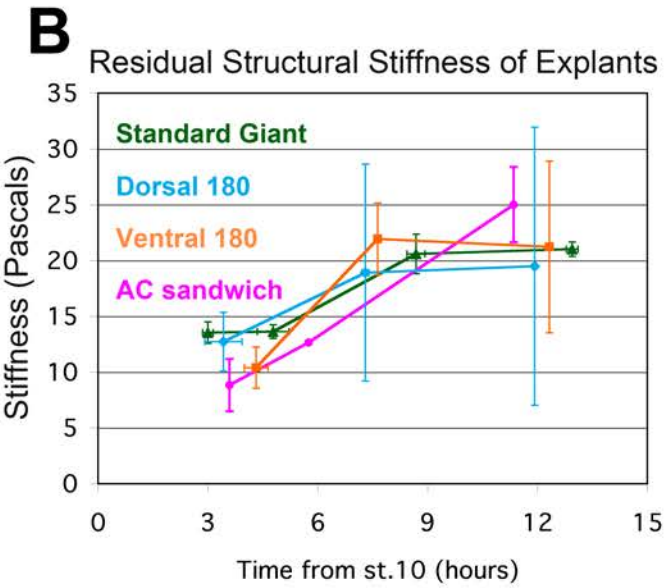

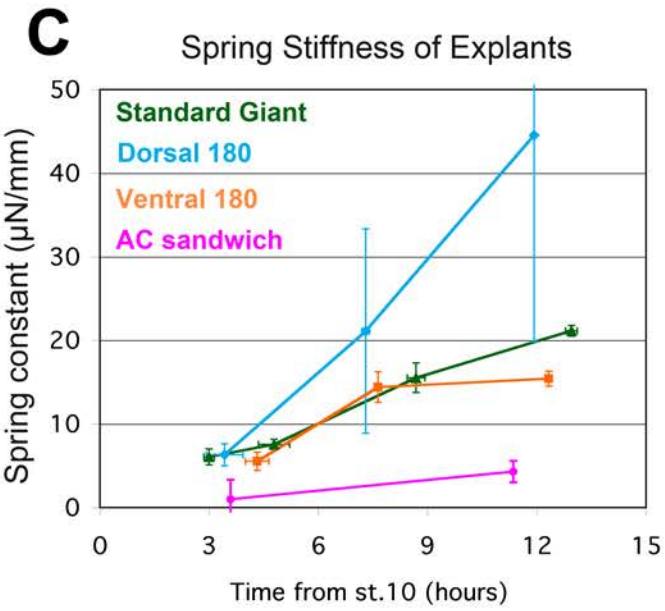

Figure 5

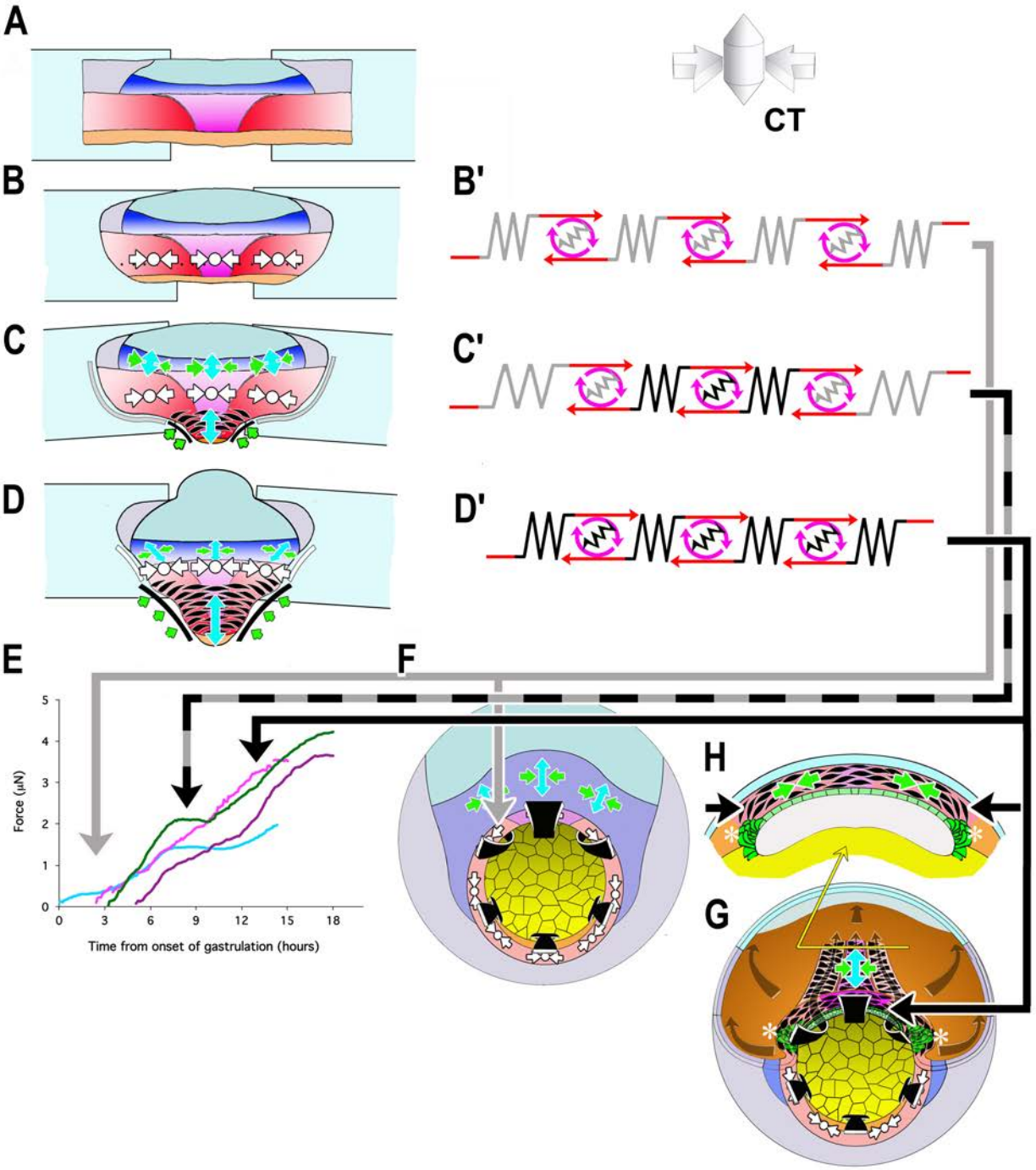

Figure 6 Shook et al.

A

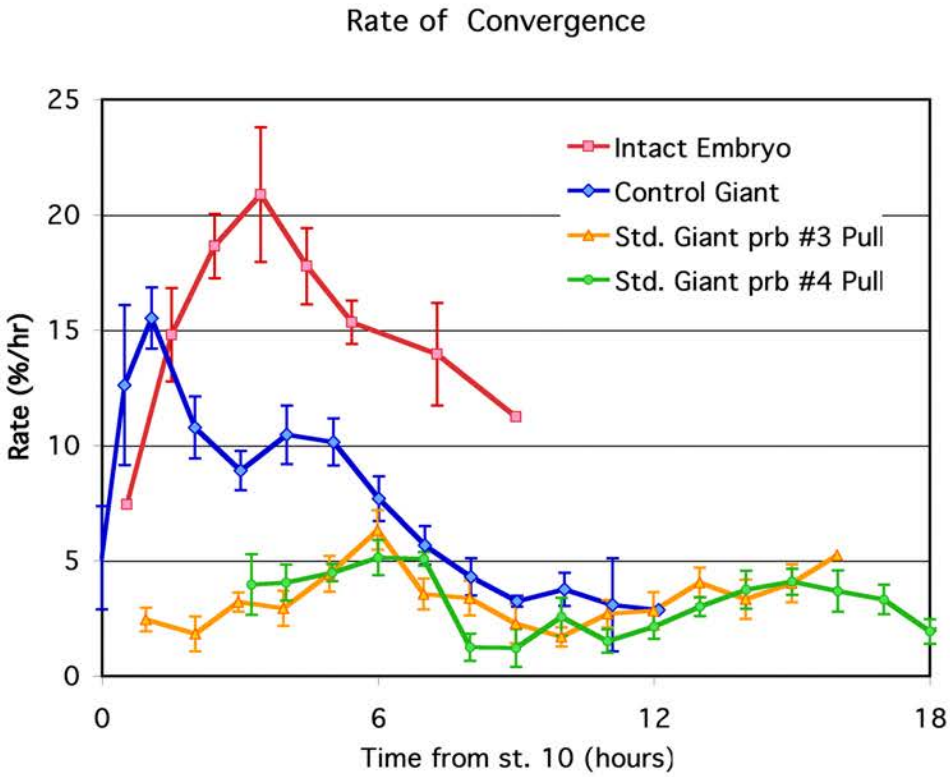

B

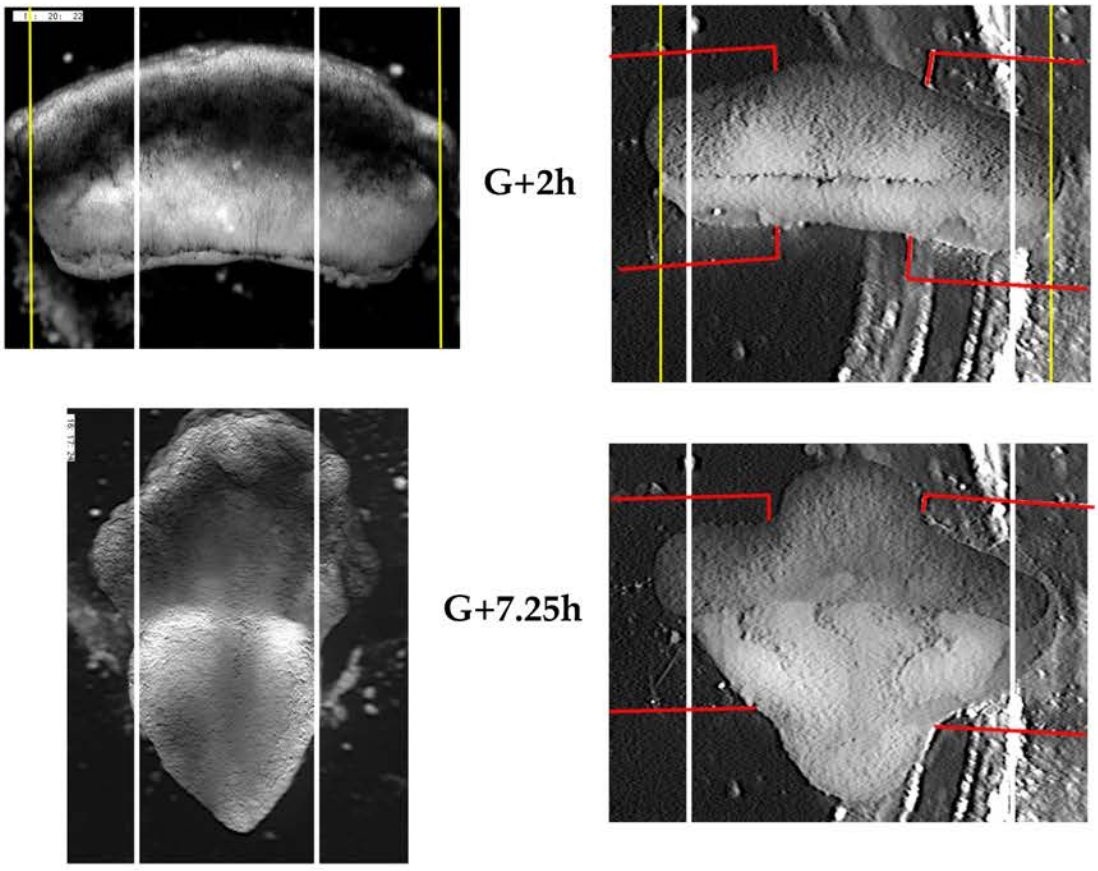

Supplementary Figure 1

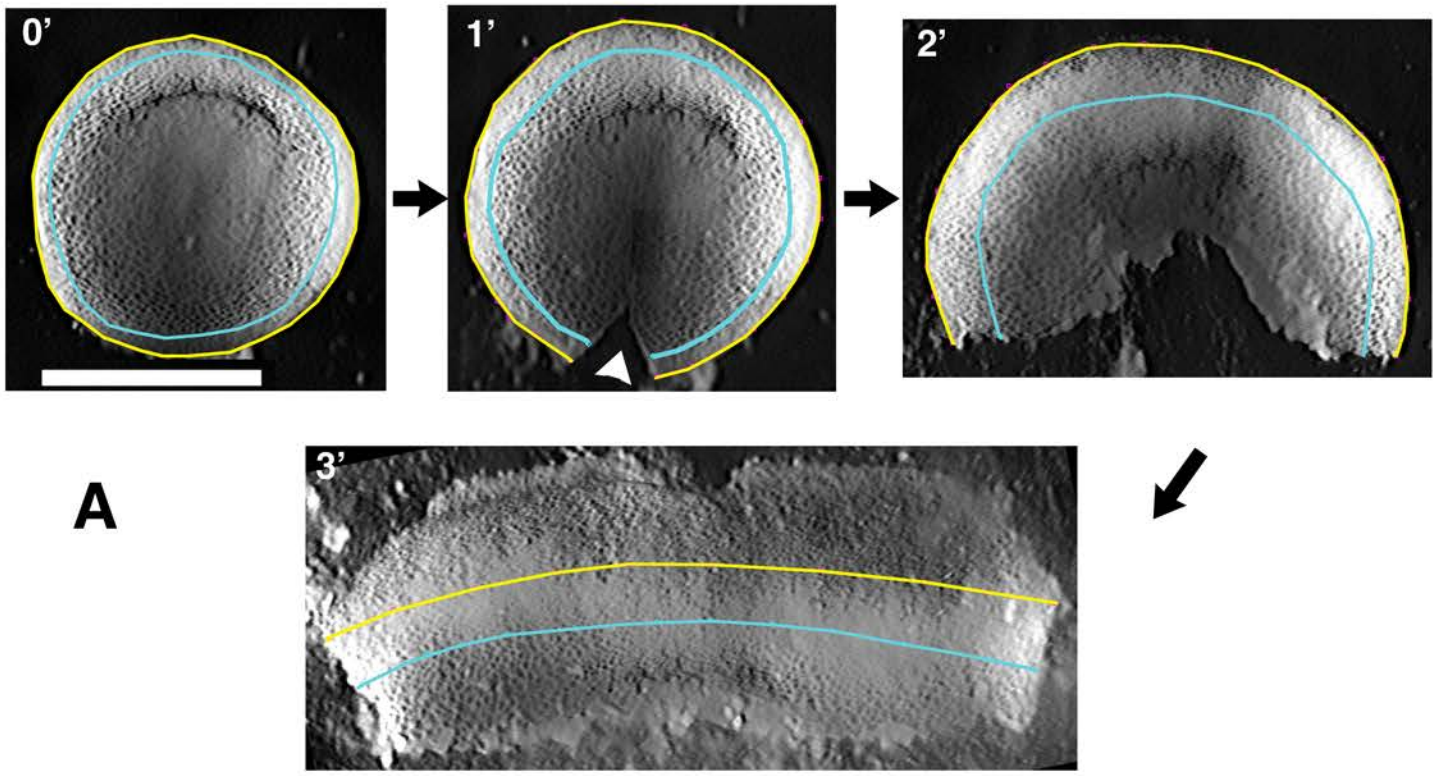

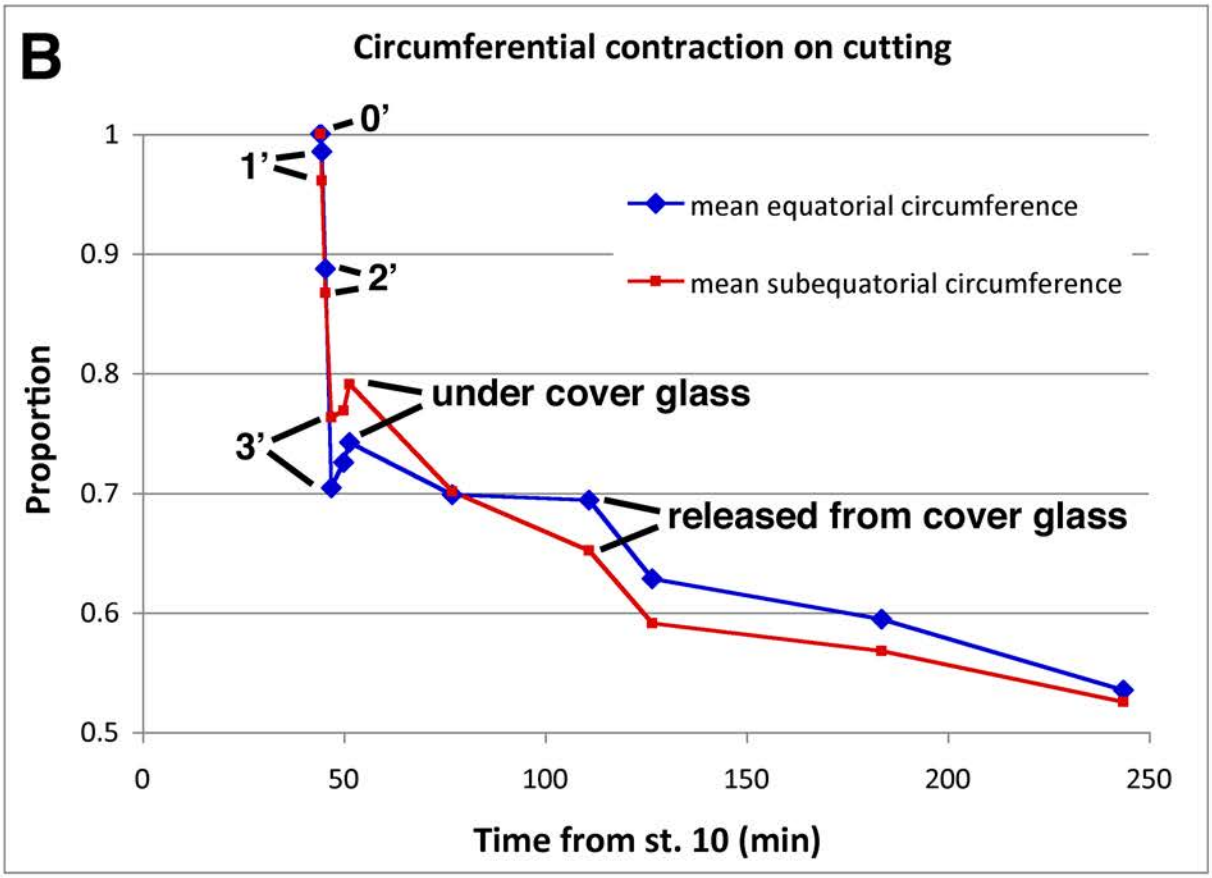

Fig. S2

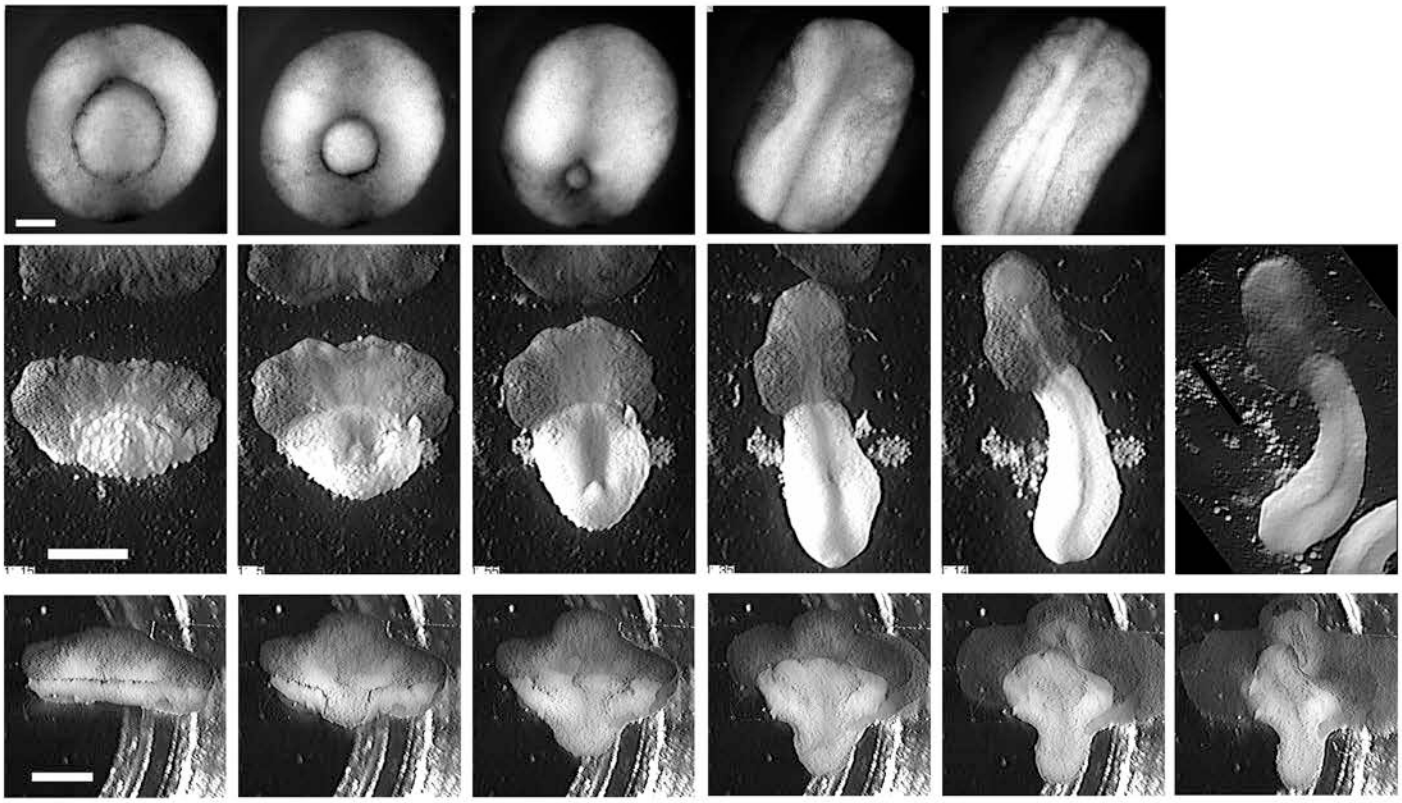

Figure S3

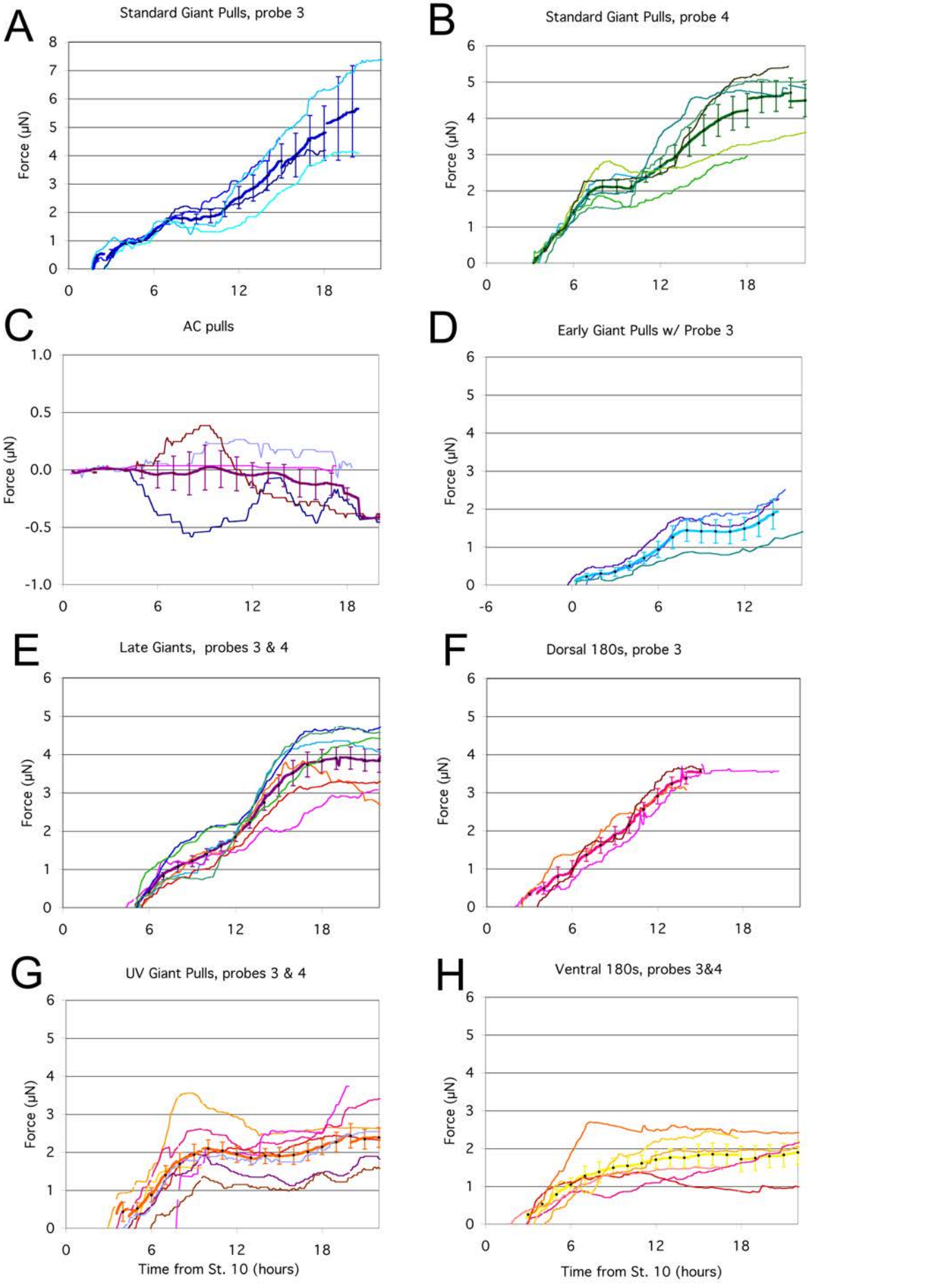

Figure S4

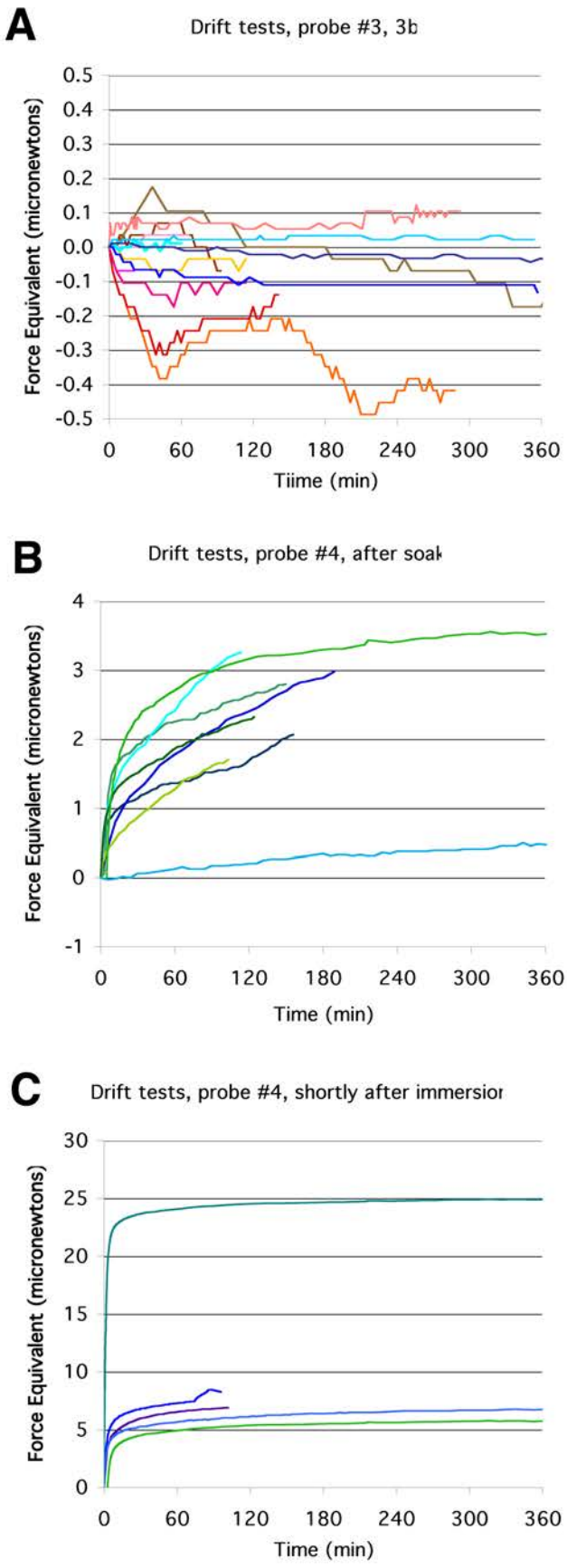

Supplementary Figure S5

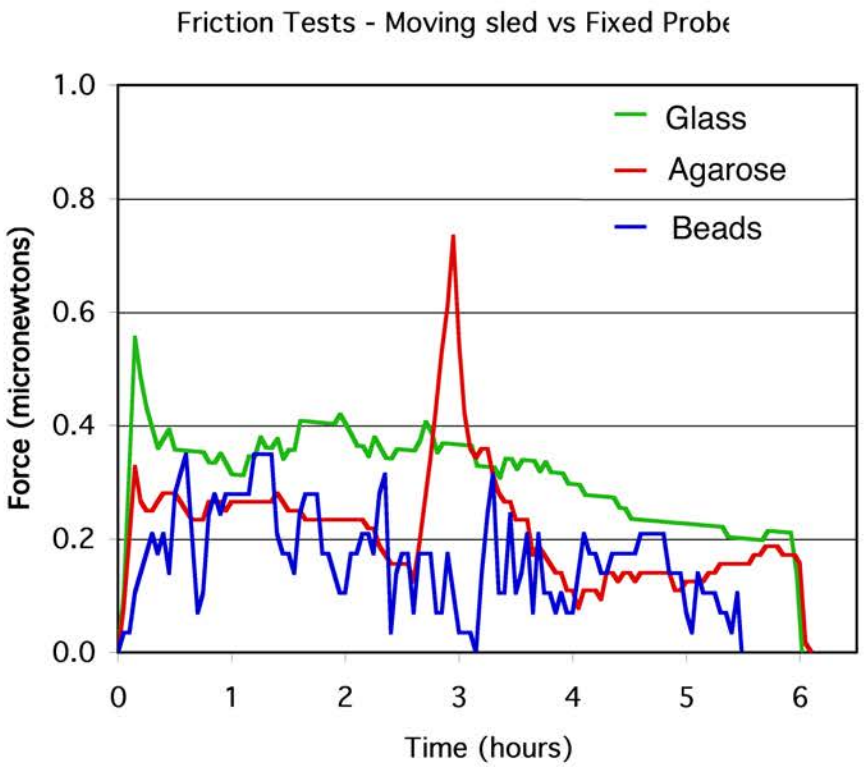

Supplementary Figure S6

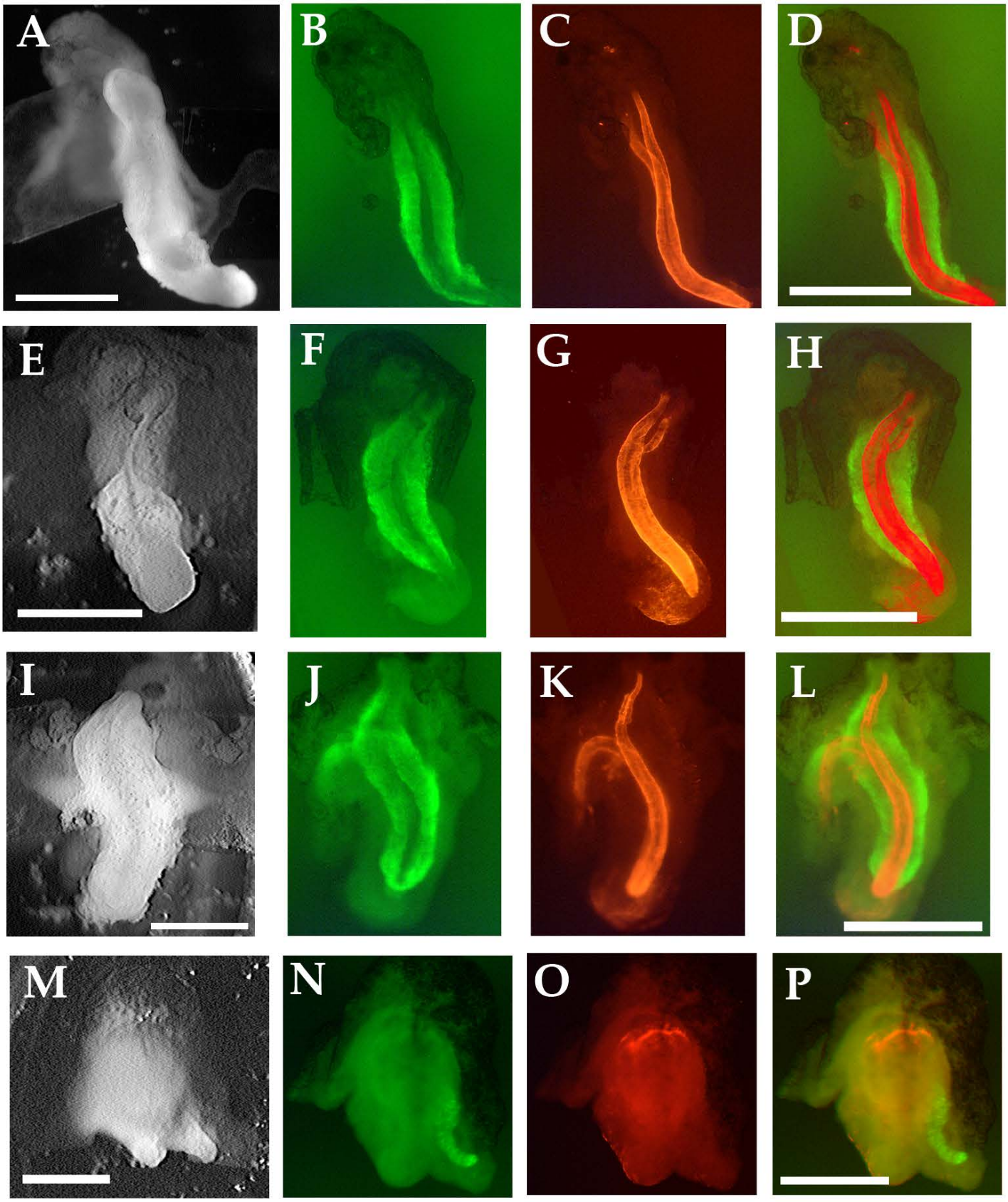

Supp. Figure S7

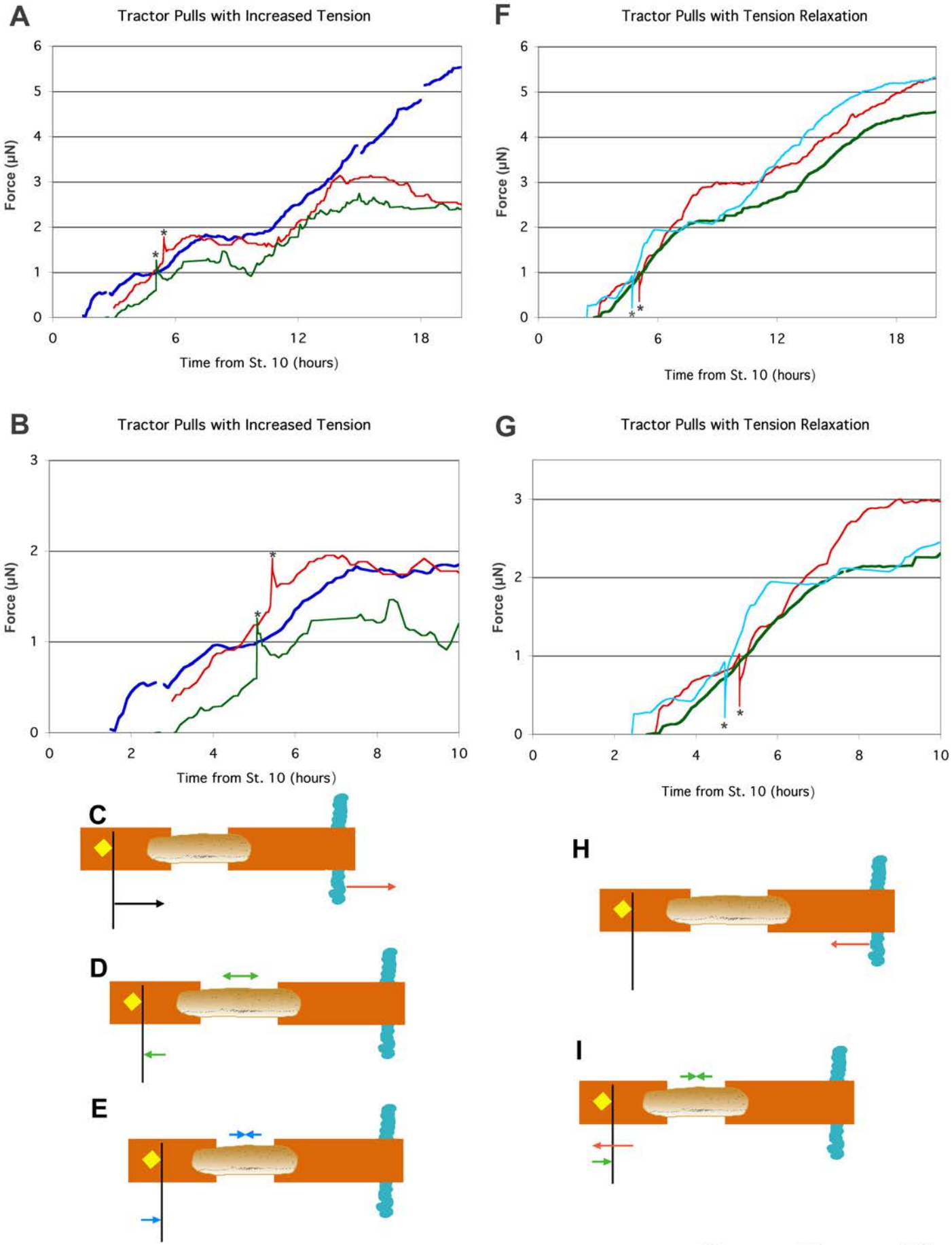

Supp. Figure S8

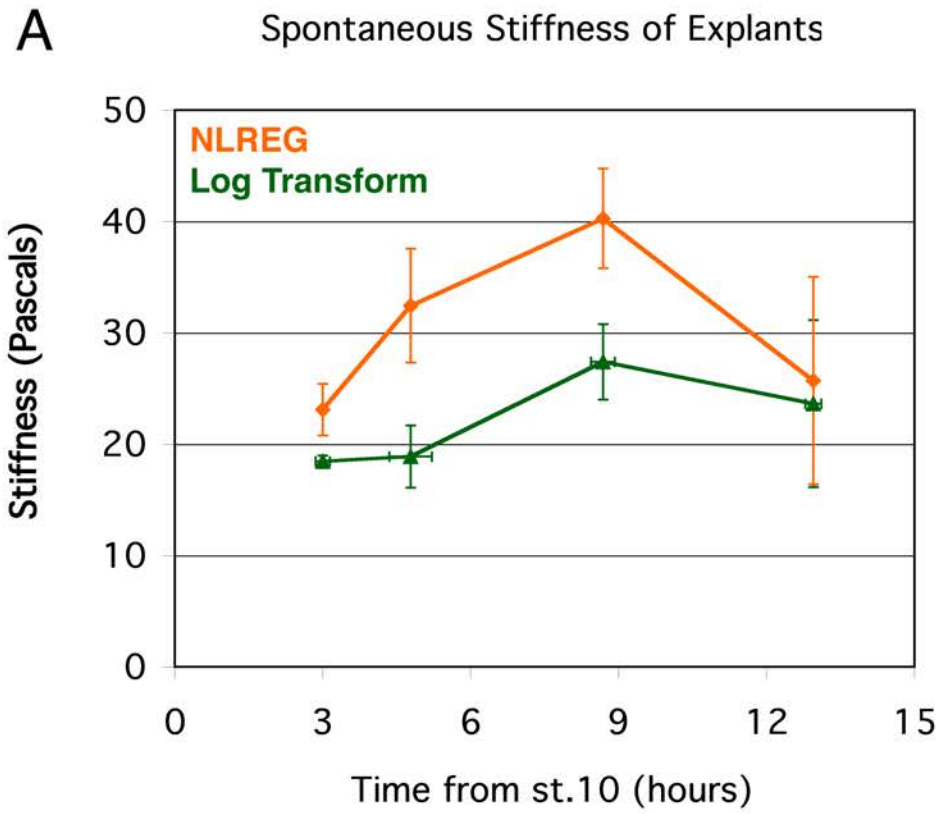

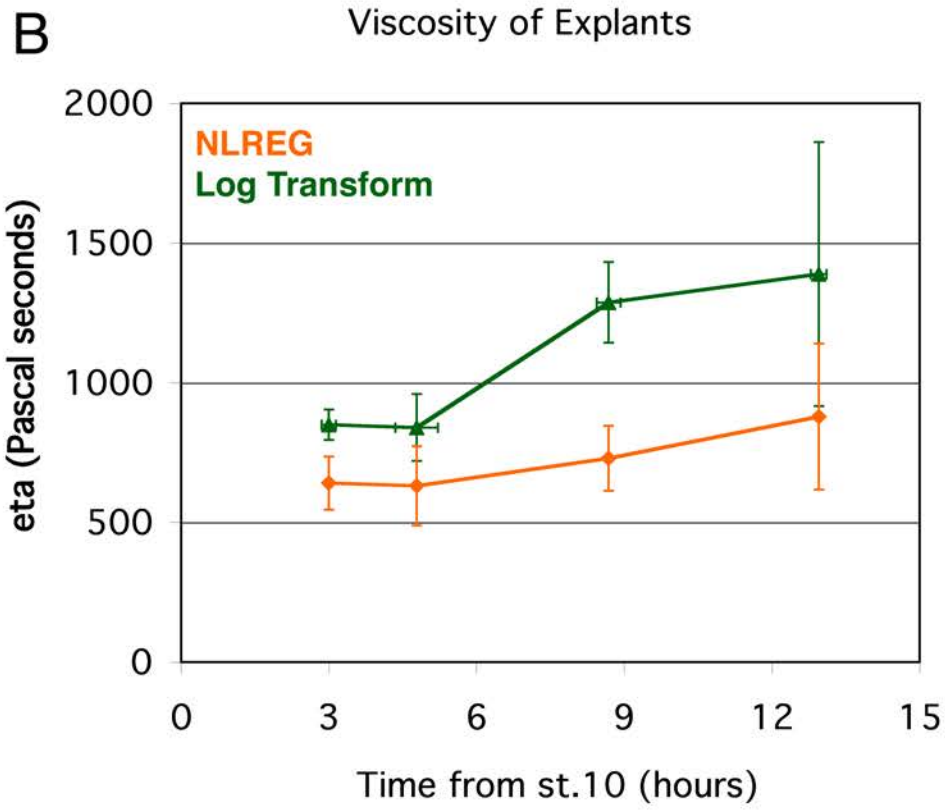

Fig. S9

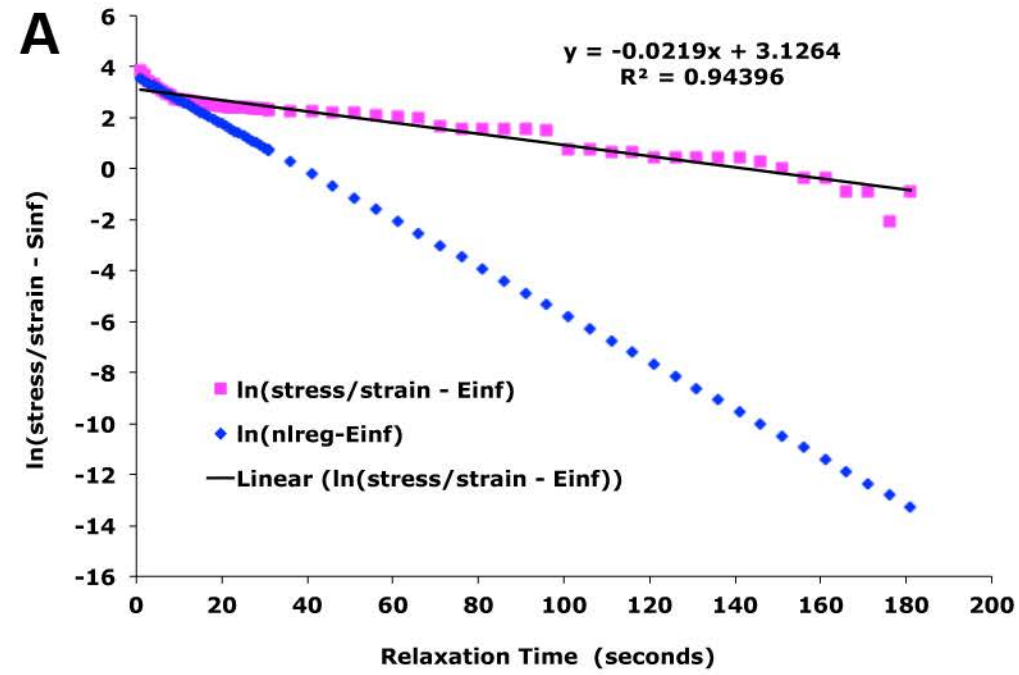

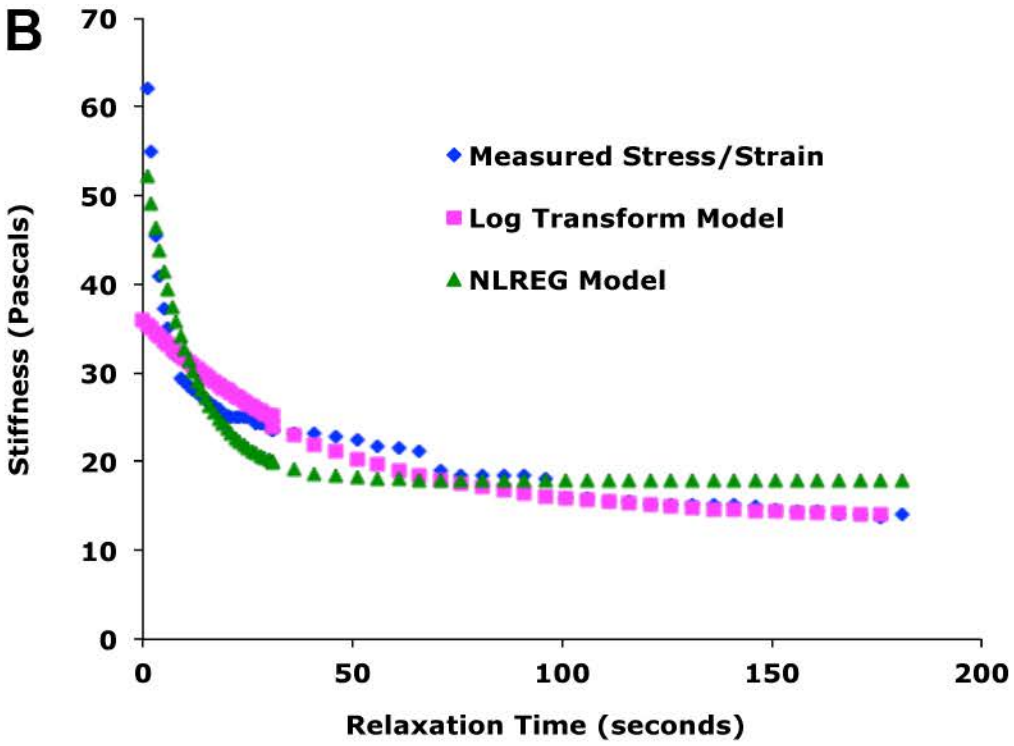

Figure S10